

JUSTUS-LIEBIG-



UNIVERSITÄT
GIESSEN

BACHELOR THESIS

IN PHYSICS

Development of a high resolution scintillation time measurement system

—
Entwicklung eines hochauflösenden Messaufbaus für
das Messen von Szintillationszeiten

submitted by

Lara Dippel

first examiner

Prof. Dr. Kai-Thomas Brinkmann

second examiner

Dr. Hans-Georg Zaunick

January 5, 2021

Abstract

Scintillators have many applications in particle physics, i. e. in the investigation of cosmic radiation, as calorimeters or for radiation protection purposes. For all applications, a detailed characterization of the scintillation material is needed. The information about the material's time response to ionizing radiation can be obtained by measuring the time spectrum, ideally with a high resolution.

This thesis is dedicated to the development of a measurement system capable of quickly and accurately determining scintillation kinetics. Optimizing the electronic and detector components, we were able to develop a coincidence measurement setup with a time resolution of 180 ps. The final setup consists of a BaF scintillator coupled to a PMT as the fixed start detector. A CAMAC CFD processes its signal with an implemented amplitude window. The stop signal of the coincidence measurement is given by a PMT coupled to the material which is to be characterized. This configuration allows us to easily measure the characteristics of different scintillation materials. However, the setup predominantly measures the prompt photons emitted by the material tested, effectively suppressing the slower components. To measure the full-timing response of the material, further adjustments to the setup are needed.

Zusammenfassung

Szintillatoren haben viele Anwendungen in der Teilchenphysik, z. B. bei der Untersuchung der kosmischen Strahlung, als Kalorimeter oder für Strahlenschutz Zwecke. Für alle Anwendungen ist eine detaillierte Charakterisierung des Szintillationsmaterials erforderlich. Die Information über das Zeitverhalten des Materials beim Durchgang von ionisierender Strahlung kann durch die Messung des Zeitspektrums, idealerweise mit einer hohen Auflösung, gewonnen werden.

Diese Arbeit widmet sich der Entwicklung eines Messsystems, das in der Lage ist, die Szintillationskinetik schnell und genau zu bestimmen. Durch die Optimierung der Elektronik- und Detektorkomponenten konnten wir einen Koinzidenzmessaufbau mit einer Zeitauflösung von 180 ps entwickeln. Der endgültige Aufbau besteht aus einem BaF-Kristall gekoppelt an einen PMT, der als fester Startdetektor dient. Ein CAMAC CFD verarbeitet dessen Signal mit einem implementierten Amplitudenfenster. Das Stoppsignal der Koinzidenzmessung wird durch einen PMT geliefert, der an das zu charakterisierende Material gekoppelt ist. Diese Konfiguration erlaubt es uns, verschiedene Szintillationsmaterialien zu vermessen. Allerdings misst der Aufbau vorwiegend die prompten Photonen, die vom untersuchten Material emittiert werden, wodurch die langsameren Komponenten unterdrückt werden. Um das gesamte Zeitspektrum des Materials zu messen, sind weitere Veränderungen am Aufbau erforderlich.

Contents

1. Introduction	1
2. Theoretical prerequisites	3
2.1. Particle interaction with matter	3
2.1.1. Interaction of charged particles with matter	3
2.1.2. Interaction of photons with matter	3
2.2. Scintillators	5
2.2.1. Organic scintillators	6
2.2.2. Inorganic scintillators	8
2.3. Photodetectors	11
2.3.1. Photomultiplier tube	11
2.4. Signal processing modules	14
2.4.1. Constant fraction discriminators	14
2.4.2. Time-to-digital converter	14
2.5. Statistical evaluation of data	15
3. High resolution coincidence measurement	17
3.1. Coincidence measurement setup	17
3.2. Optimization of electronic components	19
3.3. Optimization of detector components	23
3.3.1. Measurements with plastic scintillators	24
3.3.2. Measurements with BaF scintillators	25
3.3.3. Influence of an amplitude window	30
3.4. Final Setup	34
3.4.1. Measuring LYSO against BaF	35
3.4.2. Measuring PWO against BaF	35
4. Conclusion and outlook	39
A. Appendix	41
A.1. Additional measurement results for section 3.1	41
A.2. Additional measurement results for section 3.3.1	43
A.3. Additional measurements for section 3.3.2	44
A.4. Additional measurements for section 3.3.3	46

1. Introduction

Scintillators have a wide range of applications in particle detection. Among others, they can be used to determine the energy of ionizing radiation as well as in imaging processes for medical purposes. The detector's response to penetrating radiation strongly depends on the material's properties and particle itself. To investigate such responses, it is desirable to develop a setup with which different materials can be characterized quickly and with good time accuracy. For this purpose, a coincidence setup with a known time resolution is recommended, in which the different materials are measured against a fixed start detector. Especially in applications like *positron emission tomography* (PET), precise time-of-flight measurements are crucial since the time resolution directly corresponds to the spacial resolution. Therefore, the motivation for this thesis is the development of a coincidence measurement setup with the highest resolution achievable employing our local lab resources.

After an introduction to the theoretical background of particle detection, scintillators as well as the electronic components involved in the measurement processes, we will start with a basic coincidence setup. Throughout various measurements, the electronic components will be exchanged and adjusted to find the most suitable modules available. With this precise electronic setup, we can then proceed to find a fitting start detector. Ultimately, we will develop a configuration with which we can measure the prompt photons emitted by the scintillation process of different materials.

2. Theoretical prerequisites

2.1. Particle interaction with matter

The interaction between a particle and the detector material is the basis of particle detection. Depending on the charge, mass and energy of the particle, different kinds of interactions can occur and dominate its energy loss as it passes through matter. In the later performed measurements, muons and γ -rays are used as the ionizing radiation detected by the scintillators; therefore this section will focus on the interaction of heavy charged particles and photons with matter.

2.1.1. Interaction of charged particles with matter

The change in a particle's energy is caused by electromagnetic interactions with the electrons and nuclei of the material they traverse, such as Cherenkov and transition radiation, bremsstrahlung and ionization or excitation of atoms. Cherenkov radiation occurs when the particle's velocity is higher than the velocity of light in the medium it passes through. In contrast, transition radiation is emitted when the particle passes through the boundary between media with different permittivities. When another charged particle deflects a charged particle, it decelerates and the kinetic energy lost is converted to radiation, the so-called *bremstrahlung* [1]. The ionization and excitation processes are the biggest contributors to a heavy particle's energy loss and can be described by the *Bethe-Bloch-Formula* as follows

$$-\frac{dE}{dx} = \frac{4\pi n z^2}{m_e c^2 \beta^2} \cdot \left(\frac{e^2}{4\pi\epsilon_0}\right)^2 \cdot \left[\ln\left(\frac{2m_e c^2 \beta^2}{I \cdot (1 - \beta^2)}\right) - \beta^2 \right], \quad (2.1)$$

where $\beta = v/c$ with v as the particle's current velocity, c the speed of light, $z \cdot e$ the charge of the particle, n the electron density and I the mean excitation energy of the material. The equation therefore gives a value for the *stopping power* of a material for a charged particle in terms of its energy loss per passed distance in the material [2].

2.1.2. Interaction of photons with matter

In contrast to charged particles, which lose energy continuously over a series of the previously described processes and therefore, can penetrate the detector by a certain distance, photons are absorbed or scattered by the material in a single event. The

total amount of transmitted particles within a photon beam I while passing through an absorber material with thickness x is described by

$$I = I_0 \exp(-\mu x) , \quad (2.2)$$

where I_0 is the number of photons transmitted without an absorber and μ as the total attenuation coefficient, which includes the influences of the different possible effects that can occur, such as photoelectric absorption, Compton scattering and pair production [3].

Photoelectric absorption

The interaction between a photon and an atom can cause the full absorption of the photon, which will then disappear and cause the ejection of a photoelectron from the atom with an energy of

$$E_e = h\nu - E_b \quad (2.3)$$

with the electron's binding energy E_b and the initial photon energy given by $h\nu$, where h represents Planck's constant and ν the photon's frequency [3].

Compton scattering

Compton scattering describes the deflection of the incident photon $h\nu$ by an electron of the absorber material. The energy transfer during this process can be described by

$$h\nu' = \frac{h\nu}{1 + \frac{h\nu}{m_0c^2} (1 - \cos \theta)} \quad (2.4)$$

with m_0c^2 as the rest-mass energy of the electron, $h\nu'$ the energy of the scattered photon and θ the scattering angle. Equation 2.4 shows that even in the case of maximum energy transfer when $\theta = \pi$, the initial photon will keep some amount of its original energy [3].

Pair production

If a photon with an energy larger than 1.02 MeV, so two times the rest-mass of an electron, is in the Coulomb field of a nucleus, the photon may be converted into an electron-positron pair. This process is called pair production. In case the initial photon energy is higher than the 1.02 MeV needed, the excess energy will be equally transferred to the electron and positron as kinetic energy. The annihilation of the positron with an electron will cause the emission of two photons, each with an energy of 511 keV. Those secondary products of the interaction are also measurable by a gamma-ray detector like a scintillator [3].

2.2. Scintillators

Scintillation processes are one of the oldest and most common techniques used in particle detection and spectroscopy. It describes the production of luminescence through absorption of ionizing radiation, whereas luminescence is the emission of a characteristic light spectrum depending on the states of the excited molecules. Depending on the material used, there are different kinds of scintillators, each of which has its advantages and disadvantages when used as detectors for different applications. While charged particles cause luminescence through recombination or deexcitation after directly ionizing the scintillator's molecules, the various interactions of photons with matter discussed in section 2.1.2 result in the creation of secondary electrons, which will then be detected by the same effects as charged primary particles. Additionally, the scintillation light needs to be converted to an electrical signal, which is done by a photodetector, further discussed in section 2.3. It is also important that the complete system is light-proof, so ambient light will not interfere with the measurement. To ensure that the particle detection is as efficient as possible, the scintillation material needs to meet certain criteria.

- The conversion of deposited energy by the particle to scintillation light, also referred to as light yield, should be as efficient as possible.
- The light yield, which is defined by the number of photons per energy-deposit, should be in linear proportion to the transferred energy.
- The material should be transparent to its scintillation light, meaning the produced photons can pass through the material without exciting molecules themselves so they can reach the photodetector.
- To obtain fast signal pulses, the excitation and deexcitation processes should be as prompt as possible.
- The refractive index of the scintillator material and the photodiode should be similar enough, so the transition between the different materials does not cause light loss due to reflections.
- Similarly, the light collection should be as efficient as possible, which can be achieved by wrapping the scintillation material in reflective foil.
- Finally, the material should be chosen concerning the type of radiation that is to be detected, since different Z values will benefit the detection efficiency.

In general, scintillation materials can be categorized into organic and inorganic scintillators, which show different scintillation mechanisms that also lead to varying scintillation times. Since they are of particular interest for this thesis, the following sections will deal with those [4].

2.2.1. Organic scintillators

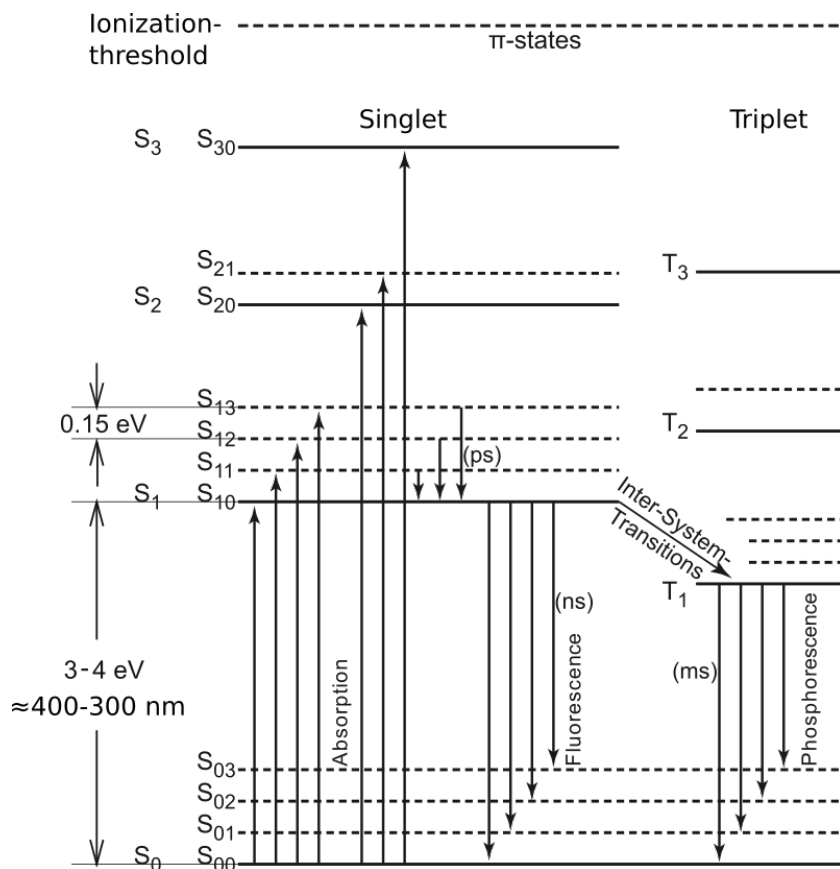


Figure 2.1.: π -electron transitions of organic molecules taken from [4]

The luminescence of a material mainly depends on its electronic structure. Thus, with organic molecules it is mostly shaped by the ground-state electron configuration of ^{12}C , namely $1s^2 2s^2 2p^2$. This configuration can change in bound states, such that a $2s$ -level can, i.e. be raised to the energy of a $2p$ -level, which would result in a $1s^2 2s^1 2p^3$ configuration. There are three possible mixed-orbit configurations, also called *hybridizations*, depending on whether the s - p -mixed orbitals are on the same energetic level (sp^3 -hybridization) or not (sp^2 - or sp -hybridization). Luminescence-producing state transitions only occur with materials in sp^2 - or sp -hybridization where at least one p -orbital remains unchanged compared to the electron configuration of the unbound atom. We call the electrons in the p -level π -electrons, whereas the electrons on mixed orbitals are called σ -electrons. Therefore, luminescence takes place between the different energetic states of the molecular π -electrons, as can be seen in figure 2.1. Here we can see that the deexcitation from a singlet state S_{1i} to S_{10} does not cause any radiation. The deexcitations from S_{10} to any state S_{0i} are responsible for prompt fluorescence and are therefore

the most important transitions when it comes to fast scintillation signals. It is also possible for electrons to perform inter-system transmissions between singlet and triplet states which cause delayed fluorescence or phosphorescence. Since they take place in time scales of micro- to milliseconds, those transitions are generally not preferred when it comes to obtaining fast signals.

What we can also see from figure 2.1 is that the produced scintillation light may re-excite electrons in the material if its energy is greater than the needed excitation energy. To prevent this and to apply the previously mentioned points made in section 2.2, materials with different properties can be added to the primary scintillation material [4].

Light yield and timing response

The light yield L of an organic scintillator is described by

$$\frac{dL}{dx} = S \frac{dE}{dx} \quad (2.5)$$

where S is the scintillation efficiency, varying between different detector materials, E the deposited energy by the particle and x the traveled distance in the material. This formula yields satisfying results for minimum ionizing particles. However, for slow protons or heavy particles with momenta smaller than 100 MeV/c, quenching effects have to be taken into account, which is described by *Birks-law*

$$\frac{dL}{dx} = \frac{S \frac{dE}{dx}}{1 + k_B \frac{dE}{dx}}, \quad (2.6)$$

with k_B as the quenching strength, which has to be obtained experimentally and is material-dependent. This law does not only describe the light yield of organic scintillators, but also applies to anorganic scintillation materials.

The timing response of organic materials is mostly shaped by prompt fluorescence so the intensity over time is given by

$$I(t) = I_0 \exp\left(-\frac{t}{\tau_f}\right), \quad (2.7)$$

with τ_f as the decay constant of the prompt fluorescence.

In the case of very fast scintillators, we also need to consider the rise time needed to occupy the excited energy states of around 100 ps. This can be described mathematically

by either adding a gaussian function or a second time constant τ_r to 2.7.

$$I(t) = I_0 \left(\exp\left(-\frac{t}{\tau_f}\right) - \exp\left(-\frac{t}{\tau_r}\right) \right) \quad (2.8)$$

or

$$I(t) = I_0 g(t) \exp\left(-\frac{t}{\tau_f}\right) \quad (2.9)$$

Similarly, the contribution of delayed fluorescence with a longer decay time τ_d can be added.

$$I(t) = I_1 g(t) \exp\left(-\frac{t}{\tau_f}\right) + I_2 \exp\left(-\frac{t}{\tau_d}\right) \quad (2.10)$$

τ_f is usually in orders of nanoseconds whereas τ_d is in orders of 100 ns – 1 μ s. The relative intensities I_1 and I_2 depend on the material [4].

2.2.2. Inorganic scintillators

With inorganic materials, the scintillation mechanisms are influenced by the material's lattice structure and dependent on the properties of the band structure and energy states in the band gaps. In non-metallic, perfect crystals the electrons are located on separated energy bands, each consisting of closely-spaced energy levels, with the *valence band* as the highest band occupied by electrons. The *conduction band* lies energetically above the valence band. In the case of perfect insulators, all energy levels of the valence band are occupied whereas the conduction band is unoccupied. Thus, the electrons are immovable.

When ionizing radiation passes through the material and deposits energy, electrons from the valence band can be excited to the conduction band, resulting in freely moveable electrons in the conduction band and holes in the valence band. With band gap sizes of 4 eV-12 eV, the scintillation light produced by recombination is outside of the visible light spectrum. To produce scintillation light inside the optical spectrum, luminescence centers, which have energy levels inside the band gap, are needed. Those can either be added by doping the material or emerge from defects in the crystal structure.

Figure 2.2 sketches the potential energy progression in a luminescence center with the lower curve describing the progression of the ground state and the higher curve the first excited state. In free space without the solid-state environment, the minima of the curves would be aligned vertically. The visible shift is caused by polarization effects in the environment and can also vary due to thermal excitations. The absorption of an electron causes the transition from A to C . The $C \rightarrow B$ transition is thermal deexcitation whereas $B \rightarrow D$ results in luminescence. Due to the horizontal shift between the two potentials, the transition does not directly happen between both minima. To excite

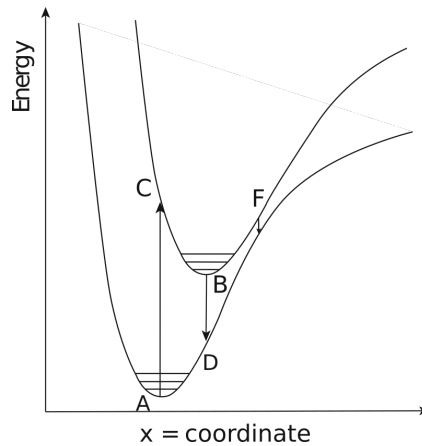


Figure 2.2.: Potentials in a luminescence center, taken from [4]. The lower curve shows the ground state and the higher curve shows the first excited state. Energy is absorbed from A to C , thermal deexcitation causes the shift from C to B . B to D is the luminescent transition. At point F the curves are close enough to cause radiation-free transmission.

an electron into the first excited state, the absorbed energy must be greater than the energy difference between the two curves' minima. Therefore, the energy emitted in the $B \rightarrow D$ transition is not sufficient to cause another excitation process. It is also possible that the deexcitation transition occurs radiation-free when the two potential curves are very close to each other, as can be seen at point F . This is called the *quench center*. A simplified display of the scintillation process can be seen in figure 2.3 which

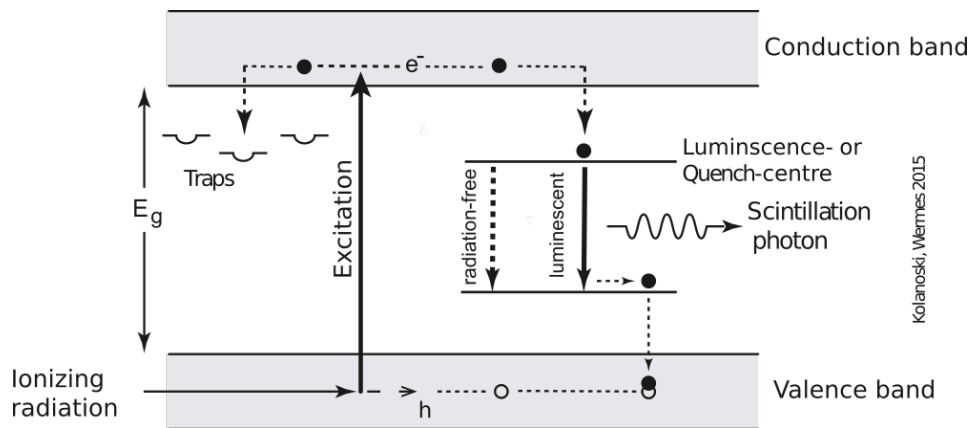


Figure 2.3.: Scintillation process in an inorganic material taken from [4].

also shows the *trapping center*, where electrons can be trapped at a certain energy level before they are thermally excited to the conduction band or transition to the valence band radiation-less.

Other phenomena that can arise in luminescence centers are *excitons* which are electron-hole-pairs whose energy levels are typically lower than the conduction band and freely

then the direct scintillation process is overlaid with the decay of a secondary center with time constants of 100 ns to 1 μ s, which is called *phosphorescence*. This is the case for most crystals utilized for their scintillation processes, and even though the interplay of effects is more complex than in the first case, the pulse shape is still sufficiently described by a sum of exponential functions including the different time constants [4].

Light yield

The light yield L of an inorganic scintillator can be reduced through quenching and trapping effects, as well as by defects and impurities in the crystal and is generally described by *Birks-law* mentioned in 2.2.1 and more specifically by

$$L = \frac{E_{\text{abs}}}{w_{e/h}} S Q , \quad (2.11)$$

where E_{abs} is the absorbed energy and $w_{e/h}$ the mean energy needed for the production of an electron-hole-pair. S describes the efficiency with which energy is transferred from electron-hole-pairs to luminescence-centers, and Q gives the probability that a center decay emits radiation. Similarly to organic materials, the light yield can be improved by doping the crystals with specific activators [4].

2.3. Photodetectors

Another vital part of the detection process is the conversion of scintillation light to measurable, electric pulses. Photodetectors utilize the photoelectric effect to achieve just that. There are different types of photodetectors, and when choosing one for a measurement setup, we should consider various factors, like the available space, the environment and the light yield of the coupled scintillator. For the measurements in this thesis, we only employ one type of photodetector, namely the photomultiplier tube, which we will discuss further in the following.

2.3.1. Photomultiplier tube

Photomultiplier tubes (PMT) are the most commonly used type of photodetectors and reliably convert even a small amount of light into measurable electric signals with low noise [4]. Figure 2.5 displays the most basic configuration of a PMT. It consists of a photosensitive layer, the *photocathode*, and an electron multiplier structure contained in a vacuum tube. The photocathode converts the incoming scintillation photons to low energy electrons through the photoelectric effect described in section 2.1.2. This

conversion can be quantitatively described through the *quantum efficiency* given by

$$\text{QE} = \frac{\text{number of photoelectrons emitted}}{\text{number of incident photons}}. \quad (2.12)$$

Most PMTs have a quantum efficiency of 20-30%. However, this efficiency also depends on the energy of the incoming photon. Therefore, different types of PMTs exist with differing responses regarding the photons' wavelengths. The electric pulses produced by the photocathode are similar in shape to the original scintillation light pulses. However, the signals are too small for direct measurement, so they are amplified by the electron multiplier section. This section consists of multiple dynodes, between which an incrementally increasing voltage is applied to accelerate electrons continuously. Through the interaction of accelerated electrons with dynodes, more electrons are being emitted and transported further along the tube. For most PMTs, this results in the production of $10^7 - 10^{10}$ electrons per scintillation pulse, which are collected and read out at the anode. In most cases, the amplification can be seen as linear. However, since the mean energy of the electrons of around 100 eV is rather low, the amplification process is sensitive to magnetic fields. Therefore, PMTs should always be shielded from stray magnetic fields that might be produced by surrounding measuring instruments [3].

Pulse Shape

The outgoing signal mostly depends on the electrons' trajectories since the photoemission itself happens within less than 0.1 ns. The *electron transit time* describes the time between the initial arrival of the photon at the photocathode and the collection of the resulting electrons at the anode and is typically around 20 ns - 80 ns. A more interesting time value for the pulse shape is the *spread in transit time* since it contains information about the signal width. This relation is further displayed in figure 2.6. To reduce the spread of transit time, optimizing the area between the photocathode and the first dynode is essential. The photodiode is slightly curved, and the distance to the first dynode is significantly larger than the distance between the dynodes, respectively. Hence, the place at which an electron is emitted from the photocathode has very little influence on its travel distance. The spread can also be reduced by high voltages between the photocathode and first dynode, as well as large differences in voltage among the dynodes. Therefore, PMTs should be run at the highest possible supply voltage.

Another factor weighing on the time resolution is the number of incident photons. Assuming the time spread complies to a normal distribution, the relative width of the transit time is proportional to $1/\sqrt{N}$ where N is the number of photoelectrons, meaning that a larger scintillator light yield will also lead to better results for timing applications. With longer scintillation decay times, the time response of most PMTs is sufficient to yield satisfying timing results. For fast scintillation times, the PMT time spread can lead to measurable influences and needs to be taken into account [3].

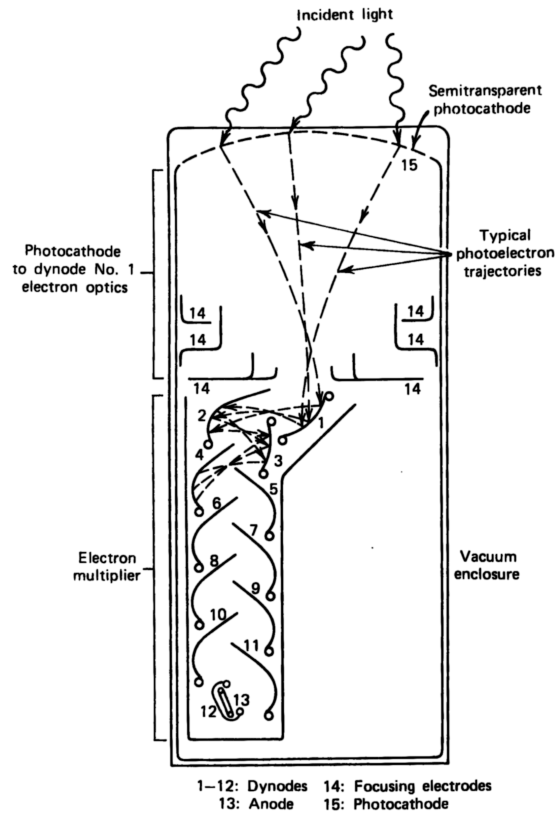


Figure 9-1 Basic elements of a PM tube. (From Ref. 1.)

Figure 2.5.: Basic components of a PMT taken from [3].

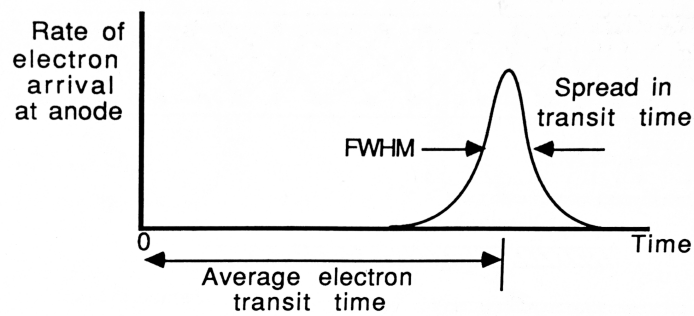


Figure 2.6.: Timing response of a PMT taken from [3].

2.4. Signal processing modules

The signals obtained by any detector need to be processed through a variety of electronic components before they can be properly evaluated and understood in a physical framework. Often utilized functions, like discriminators and logic gates, are combined into modules with standardized signal levels and shapes. For analogue and logic signals, NIM (Nuclear Instrumentation Module) modules are used, whereas CAMAC (Computer Applications to Measurement and Control) modules are applied for digital control and readouts. The different kinds of modules can be configured according to the desired experiment.

Every signal-modification has an effect on the signals shape, timing and amplitude, which need to be considered, especially in high-resolution measurements.

2.4.1. Constant fraction discriminators

Discriminators convert analogue signals into logical ones, usually when the incoming signal amplitude surpasses a certain threshold. There are different factors weighing in on time-resolution, such as the amplitude noise and walk. Those influences are minimized in a *constant fraction discriminator* (CFD). Here, the threshold is not given by a constant amplitude but rather by a constant fraction of the maximal amplitude. The triggering process is shown in figure 2.7, where the initial signal is separated into two parts. One part of the signal U_F is inverted and scaled-down such that the maximum amplitude corresponds to the threshold level. The other part's amplitude U_T is left unchanged but delayed, so the constant fraction of the rising edge aligns with the maximum of the inverted signal. Adding those results in a bipolar signal U_Z , which will trigger the output U_a when crossing zero [5]. During this project, two different kinds of CFDs are used. One of them is a NIM CFD where the thresholds can be adjusted continuously, but the delay time is fixed. The second one is a CAMAC CFD with threshold levels between 7 mV and 990 mV and an adjustable delay time, which is set to 2 ns unless stated differently.

2.4.2. Time-to-digital converter

Time-to-digital converters (TDCs) are employed to measure the time difference between two events. The TDC used in this thesis is a *TDC7200* by *Texas Instruments* with a nominal time-resolution of 55 ps. The TDC has an automatic self calibration functionality built into it to achieve this time accuracy. It receives two different logical signals serving as the start and stop signal for the measurement and is run in measurement mode 2, so the minimal and maximal time between a start and stop signal are given by

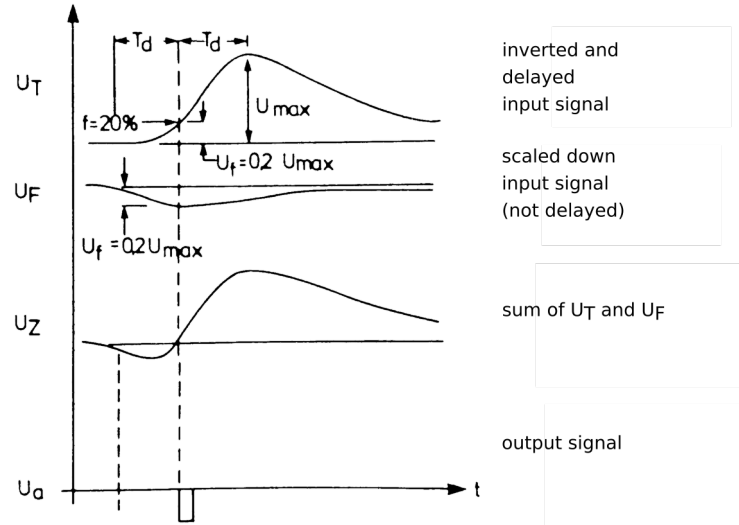


Figure 2.7.: Signal processing of a CFD taken from [5]

the clock time t_{CLOCK} with

$$t_{\min} = 2 \times t_{\text{CLOCK}} \quad (2.13)$$

$$t_{\max} = (2^{16} - 2) \times t_{\text{CLOCK}} . \quad (2.14)$$

Since all measurements are performed with a clock time of 6.25×10^{-8} s this results in $t_{\min} = 1.25 \times 10^{-7}$ s and $t_{\max} = 4.1 \times 10^{-6}$ s. Especially t_{\min} will be an important aspect to consider in the course of this study.

Furthermore, the time overflow is set to 2 μ s, so all measurements longer than that will automatically be discarded, and the timer will be reset.

For more information about the TDC its datasheet can be found in the Bibliography [6].

2.5. Statistical evaluation of data

The data received by the TDC consists of the measured time differences. To evaluate the time differences between the start and stop signals, they are plotted as a histogram such that the distribution of the measured time differences is displayed. To gather information about the time spread, we need to fit the data with an appropriate theoretical distribution. For the types of timing measurements performed in this thesis, we can generally assume a gaussian distribution. Therefore, we obtain the time spread through the standard deviation σ of the fitted function [3].

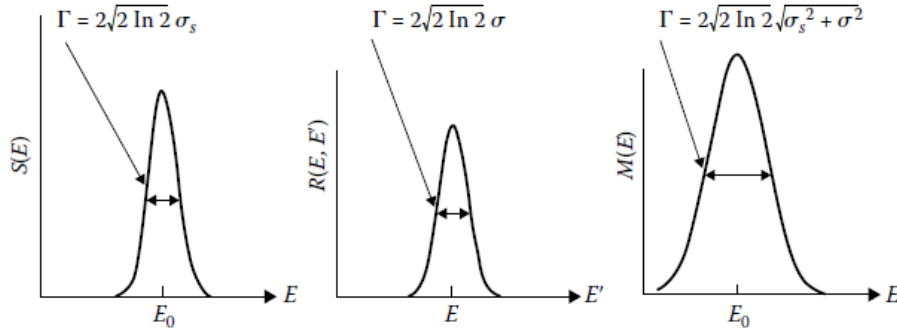


Figure 2.8.: A gaussian distribution folded with a different gaussian distribution results in another gaussian distribution, taken from [7]

However, every component of the measurement setup will lead to small deviations that can be described by a gaussian distribution. The fitted curve of a measurement thus portrays a convolution of multiple distributions. To obtain information about the influence of a single component, this fit needs to be deconvolved. In the case of a folding of two gaussian distributions, the relation between the individual distribution widths is shown in figure 2.8 and given by

$$\begin{aligned} \Gamma_{\text{total}} &= \Gamma_1 + \Gamma_2 \\ &= 2\sqrt{2\ln(2)}\sigma_1 + 2\sqrt{2\ln(2)}\sigma_2 = 2\sqrt{2\ln(2)}\sqrt{\sigma_1^2 + \sigma_2^2} \end{aligned} \quad (2.15)$$

or for the standard deviation itself $\sigma_{\text{total}} = \sqrt{\sigma_1^2 + \sigma_2^2}$ respectively [7].

With this in mind, we can perform a series of measurements to determine the individual influences on the time spread of the components, which the following chapter will deal with.

3. High resolution coincidence measurement

The central focus of this thesis is the development of a coincidence measurement system with a high time resolution for an as precise as possible scintillation time measurement. To achieve this, we start with a basic time coincident measurement setup which we will then optimize through various adjustments to its components.

3.1. Coincidence measurement setup

The simplest setup to measure the coincidence between two detectors is shown in figure 3.1. Assuming the same particle passes through and is detected by both detectors, we can measure the difference in time between the two registered events. Since electronic measurement devices have limitations concerning the minimal time difference between two registered events, the signal which will serve as the stop signal is delayed by a fixed amount of time. Subtracting this delay from the measured time difference will then yield the time difference of the detection process.

This time difference is influenced by several factors, like the size and position of the detectors, delays and time jitters caused by the electronic components, as well as the different scintillation times depending on the material. Since the goal is to measure the latter, other possible influences should be minimized. The easiest optimization in a lab environment is the physical arrangement of the detectors. In every measurement performed for this thesis, all detectors were as close as possible to each other, so the impact of time-of-flight differences caused by the distance between the detectors is negligible.

The first measurements are performed with two barium-fluoride (BaF) scintillators attached to PMTs, stacked on top of each other. Since the crystals used are relatively large, we add two smaller plastic scintillators to the setup. Those are positioned above and under the BaFs respectively, so the angular distribution of particles that will be detected by all four detectors is small, and the resulting time-of-flight differences are also negligible.

The electronic schematic is shown in figure 3.2. Here, all detector signals are processed by the same NIM CFD module. The thresholds are low and set in such a way that the rates for each detector of the same type are similar. Since we measure coincidences, the thresholds do not need to cut off all noise. The plastic detector signals are connected with a logic gate which can be changed between an AND and OR logic. This output

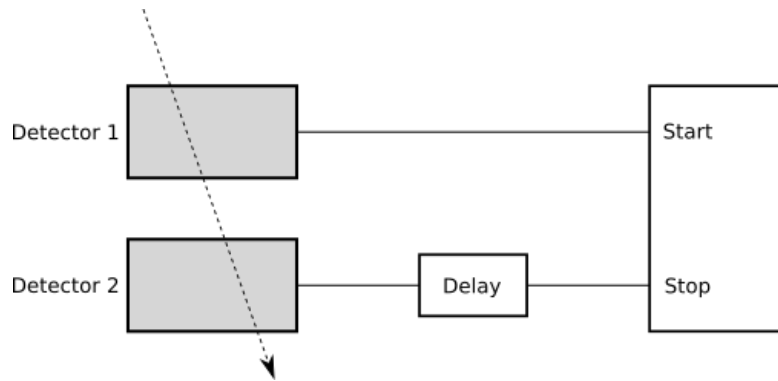


Figure 3.1.: Schematic of coincidence time measurement between two detectors. Detector 1 will trigger the start of a timing measurement which will be stopped by detector 2. In respect to the time resolution of the electronic timing device, the stop signal has to be delayed.

then triggers the gate generator. If a signal from the BaF 1 detector arrives within the open gate, then the signal gets converted from NIM to TLL and serves as the start of the measurement. To compensate any delays caused by electronic components of the gate generation, the BaF 1 signal is delayed with an active delay by 46 ns.

The BaF 2 signal is delayed by the same active delay module but by 192 ns to compensate the minimal time difference needed by the TDC and additional delays caused by electronics. After the conversion to TLL, the BaF 2 signal stops the measurement.

This setup is used in two different configurations. The previously described version is used for true coincident measurements between all four detectors. This is labelled as *Setup 2*. For a quicker evaluation of the time resolution, we use *Setup 1*. Here, the BaF 1 detector output is split and plugged into the CFD for the start and stop signal. In this case, the time jitter is only dependent on the scintillation kinetics of one detector.

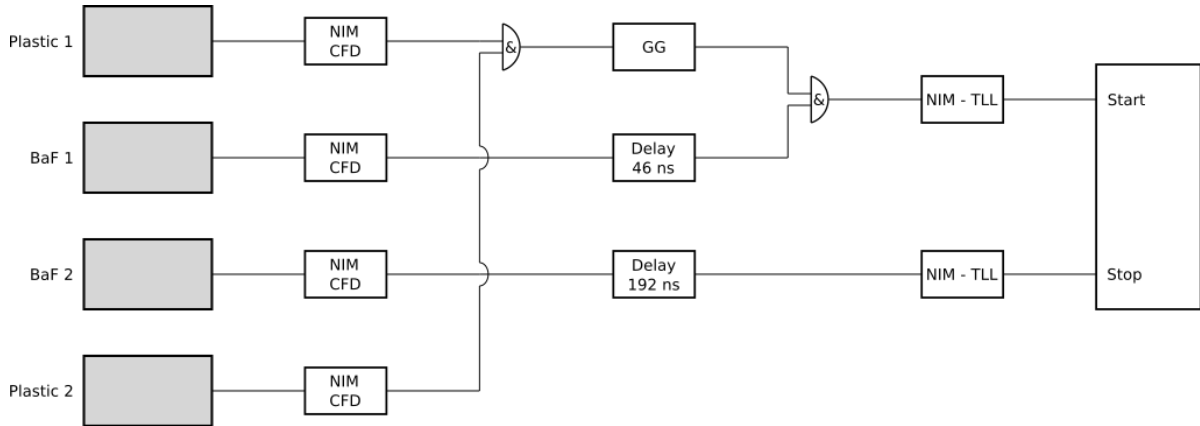


Figure 3.2.: Schematic setup of the electronic components used for the first coincidence timing measurements. The same NIM CFD module processes all incoming detector signals. The logic-gate between the two plastic detectors opens a gate with which the signal from BaF 1 needs to correspond to function as the start signal. The BaF 1 signals are delayed by 46 ns to compensate any time delays arising from the gate generation. The BaF 2 signal is delayed by 192 ns required for the minimum time difference needed by the TDC and slowed down start signal transmissions.

3.2. Optimization of electronic components

Setup 1 is tested with different active delay NIM modules to identify the best unit available in our lab. The results are displayed in table 3.1 with the corresponding histograms that can be found in the appendix at A.1. The best time resolutions are achieved with the delay modules labelled *Delay 2* and *Delay 3* and the CFD thresholds for the BaF 1 signals set as low as possible. This yields a standard deviation of about 150 ps (see figure 3.3) or 156 ps (see figure 3.4), respectively. The two plastic detectors are connected by a logic *OR*. Since *Setup 1* does not measure coincidences between two different detectors, any time-of-flight influences due to the angular distribution of incoming particles can be discarded, so the coincidence between the plastic detectors is not needed.

figure	delay module	entries	time resolution [ps]
3.3	2	3577	150
3.4	3	630	156
A.1	4	1719	179

Table 3.1.: Comparison of the time resolutions for different delay modules used in setup 1 with an OR-connection between the two plastic detectors.

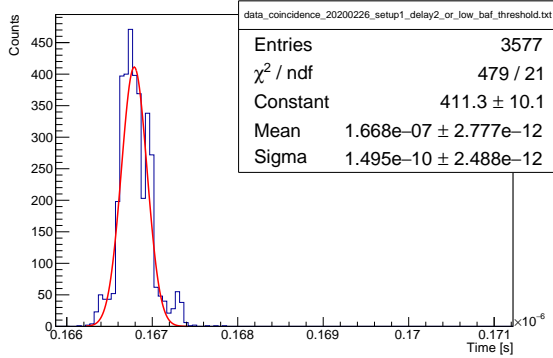


Figure 3.3.: Setup 1 with delay module 2 and OR connected plastic detectors yields a time resolution of about 150 ps.

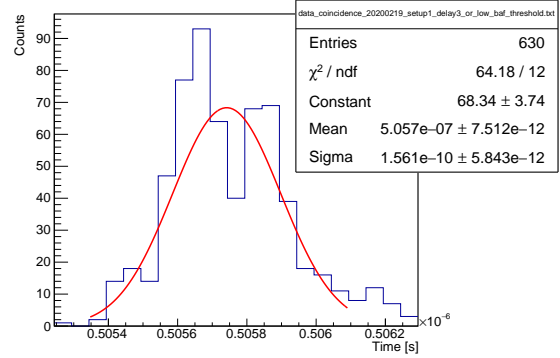


Figure 3.4.: Setup 1 with delay module 3 and OR connected plastic detectors yields a time resolution of about 156 ps.

figure	delay module	plastic connection	entries	time resolution [ps]
A.2	2	OR	1006	420
A.3	3	OR	1812	495
A.4	4	OR	2732	466
3.5	2	AND	768	301
A.5	4	AND	3933	403

Table 3.2.: Comparison of the time resolutions for different delay modules used in setup 2 varying between *AND* and *OR* connection between the two plastic detectors.

Performing the same type of measurements with *Setup 2* we obtain the results shown in figure 3.2. Here, the *Delay 2* yields the best results, especially with the *AND* connection between the plastic scintillators (see figure 3.5). From now on, we will identify *Delay 2* as the best available active delay module for this project.

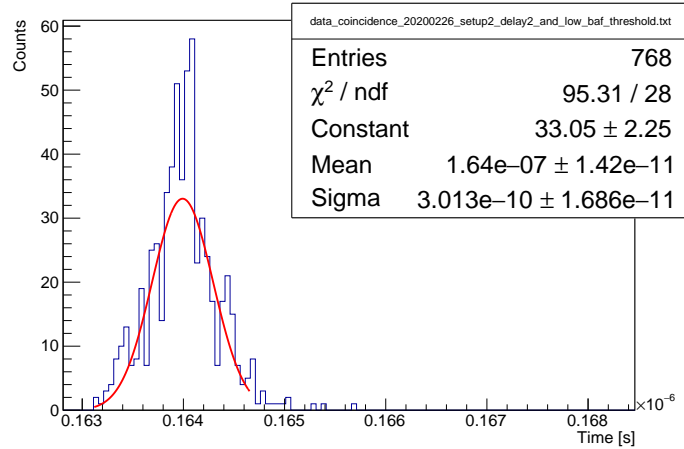


Figure 3.5.: Setup 2 with delay module 2 and AND connected plastic detectors yields a time resolution of about 301 ps.

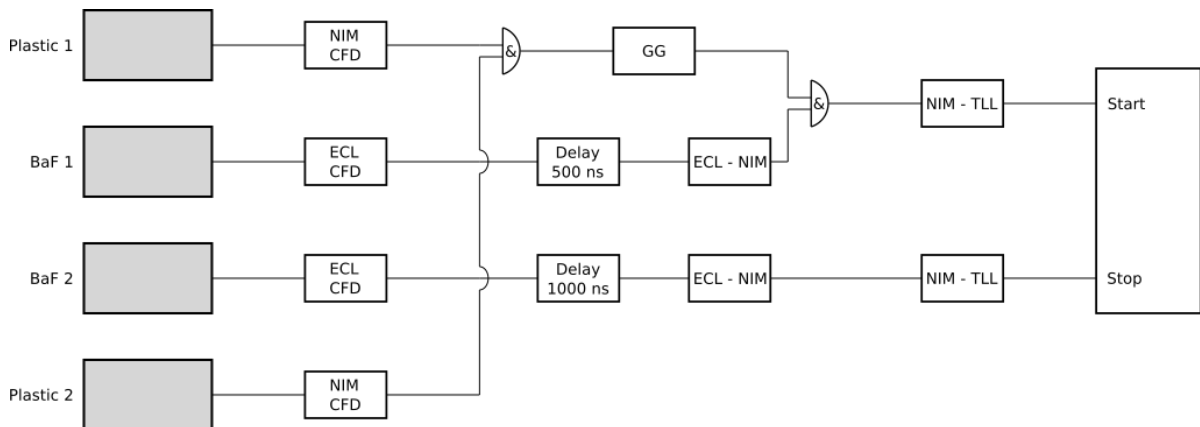


Figure 3.6.: Schematic setup of the electronic components used in *Setup 3*. The plastic detector configuration is the same as in *Setup 1* and *Setup 2*. The two BaF detector signals are now processed by a CAMAC CFD module with adjustable thresholds and then delayed by a CAMAC Delay module. The delay time is fixed to 500 ns for the BaF 1 signal and 1000 ns for the BaF 2 signal. Before they start and stop the TDC measurement, both signals have to be converted from ELC to NIM and from NIM to TLL, respectively.

As a next optimization step, we change the NIM CFD module used in *Setup 1* and *Setup 2* to a CAMAC CFD. The new setup, which from now on will be labeled as *Setup 3* is sketched in figure 3.6. In addition to the CFD module, we also switch to CAMAC delays. Those are not adjustable like the previously used NIM modules but fixed to a delay time of 500 ns. The start signal still has to be delayed by one iteration of the module to compensate for any delays in the gate generation. With regard to the TDC,

the stop signal is delayed by two iterations of the delay module, summing up to 1000 ns. Table 3.3 shows the comparison between the time resolution of *Setup 2* and *Setup 3*. We can clearly see that *Setup 3* yields a much better time resolution with about 191 ps.

figure	CFD type	entries	time resolution [ps]
3.5	NIM	768	301
3.7	CAMAC	627	191

Table 3.3.: Comparison between the *Setup 2* and *Setup 3*. In both measurements the plastic detectors are AND connected and the detection rates are similar.

To evaluate the time jitter only caused by the electronic components, without the influence of the scintillators, we use a similar method as before with *Setup 1* and again, split the output signal from BaF 1 to use it as the start and stop of the measurement. This is labeled as *Setup 4* and is displayed in figure 3.8. What we notice here is that the time resolution of 48 ps is in the same order of magnitude as the TDC time binning of 55 ps. Therefore, the TDC binning is not fine enough, which causes the "dip" in the peak of the distribution shown in figure 3.8. This also means that the electronic components in this setup cannot be optimized any further with the employed TDC.

With this knowledge, we can now move on to develop a setup which allows the fast and precise measurement of scintillation kinetics for different detector samples.

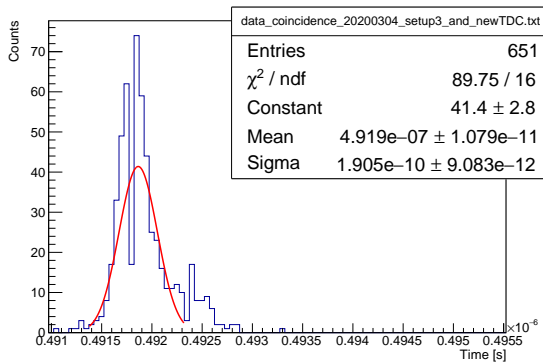


Figure 3.7.: Setup 3 with AND connected plastic detectors yields a time resolution of about 191 ps.

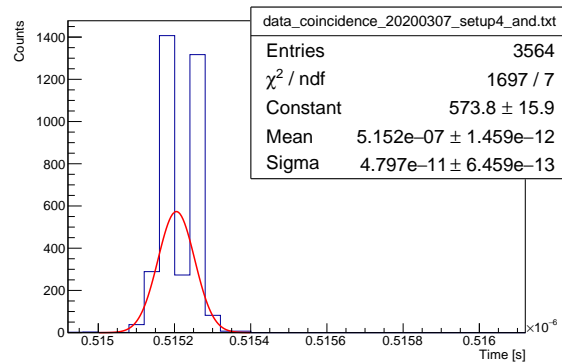


Figure 3.8.: Setup 4 with AND connected plastic detectors yields a time resolution of about 48 ps. This measurement also serves as a characterization of the time resolution of all electronic components used in this configuration.

3.3. Optimization of detector components

The ideal configuration to quickly measure scintillation kinetics for different materials is to have one reference detector with known scintillation decay times and an unchanging electronic setup with a known time resolution. Since we have identified the ideal electronic components in the previous section, we will now perform a series of measurements to find a suitable start detector.

As a first optimization step, we now use plastic detectors with a smaller volume. On the one hand, it allows us to remove the two previously used plastic detectors from the setup since the time-of-flight differences caused by the particles' angular distribution is now negligible. Additionally, the travel distance of produced photons in the detector is also reduced for smaller crystals. On the other hand, the total energy deposit in the detector is also smaller.

Another change to the setup is that instead of using cosmic rays, we employ a source in the measurements, which greatly reduces the measurement time needed to acquire sufficient statistics.

The from now on used setup schematic is shown in figure 3.9. All modules used are the same as in the previous configuration. Since the removed plastic detectors also provided the coincidence condition, the gate in which the start and stop signal have to occur is now opened by the start detector (*Detector 1* in figure 3.9). The same detector also starts the measurement whenever an output signal that meets the CFD threshold is produced. However, not every signal corresponds to a coincidence. To rule out single and random events, the TDC time overflow is set to $2\ \mu\text{s}$. With this new configuration, we perform another measurement to evaluate the time resolution. The *Detector 1* signal is split at the output and plugged into both CAMAC CFD channels. The thresholds are set to the same value. This leads to a time resolution of 76 ps as can be seen in figure 3.10.

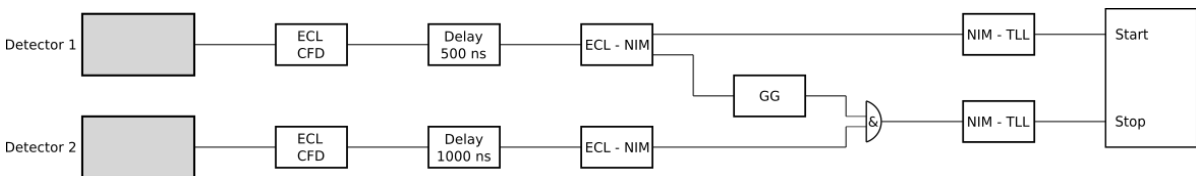


Figure 3.9.: Schematic setup of the electronic components used for the coincidence timing measurements. Both detector signals are processed by the same CAMAC CFD and delays. *Detector 1* serves as the start detector and therefore triggers the NIM gate generator after the signal conversion. The *Detector 2* signal is delayed by 500 ns in respect to *Detector 1*. If occurring in the time window set by the gate generator, the delayed *Detector 2* signal stops the measurement.

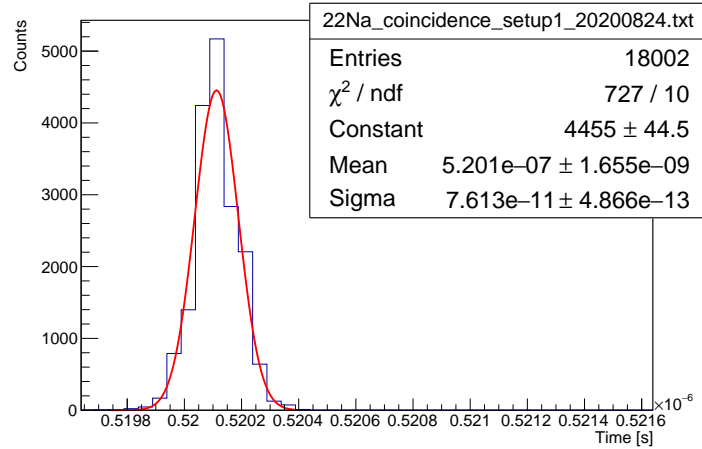


Figure 3.10.: Measurement to characterize the time resolution of the electronic components for the new setup shown in figure 3.9. The time resolution is about 76 ps.

3.3.1. Measurements with plastic scintillators

With the known time resolution of the electronic components, we can now measure the coincidence time between two plastic detectors. Each of them is coupled to a PMT, and we assume both detector systems to be identically constructed, so they influence the time spread equally. For the first measurement, we use a ^{22}Na source and position it between the two detectors. Ideally, each detector will then measure one of the 511 keV annihilation photons following the β^+ -decay of the source.

The resulting time distribution is shown in figure 3.11. What we can see here is that the distribution is spread over about 6 ns. A Gaussian fit to the center peak leads to a time resolution of 474 ps. However, it is not entirely clear from where the spread in the distribution originates. Since the time resolution of the electronic components is significantly better, and the distribution itself is a sharp peak, electronics can be ruled out as a factor. Multiple measurements were performed with this setup, making sure no faulty connections or missing terminations cause the wide time spread. The histograms in the appendix (A.7-A.10) show that none of our modifications to the setup improved the results in any significant way.

A reason for the broad distribution could be that the 511 keV photons do not have enough energy to cause a sufficient number of prompt photon emission in the detector. The distribution is then also heavily influenced by the photons emitted through slower decay channels of the scintillator. To test this theory, we perform the same measurement with higher energies. In this case, we switch to cosmic radiation, so the detectors are now stacked over each other again. The measurement with cosmic radiation and the two plastic detectors leads to the distribution shown in figure 3.12. We can see that the overall spread is reduced to about 4 ns and a gaussian fit to the peak yields a time reso-

lution of about 387 ps. This slight but visible improvement to the distribution validates our assumption that the low photon energy leads to unsatisfying results. However, even with high energy cosmic radiation, the here obtained resolution, especially compared to the electronic resolution of 76 ps, is not sufficient for high-resolution measurements of scintillation kinetics. We, therefore, disregard the plastic scintillators and proceed with BaF detectors in the next steps.

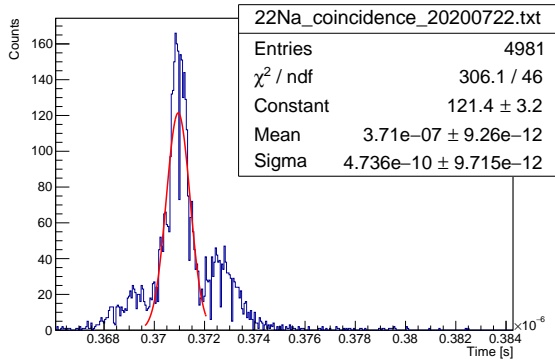


Figure 3.11.: Measurement with setup shown in 3.9 where both detectors are plastic scintillators. A ^{22}Na source is used. The time resolution is about 474 ps. However, the fit only describes the center peak of the distribution. Including the total time spread, the distribution spans over 6 ns.

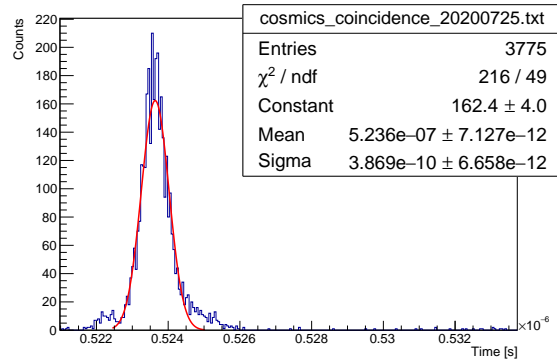


Figure 3.12.: The histogram shows the time distribution when measuring coincidences between two plastic detectors with cosmic radiation. This leads to a time resolution of 387 ps.

3.3.2. Measurements with BaF scintillators

The following measurements are performed with a BaF detector with a smaller crystal attached to a PMT. The scintillation material contains different components that filter out the longer scintillation decay times. With this feature in a start detector, we should be able to achieve higher resolutions because only the prompt photons will start the timing measurement.

For the stop signal we use the Hamamatsu multianode PMT (from now on shortened to mPMT) type H6568, H6568-10 [8] with 16 readout channels. The mPMT is not coupled to any scintillating material. Therefore, the following measurements will give a direct indication on the time resolution of every setup component, which will be used in an actual kinematics measurement, without the influence of an additional scintillator.

For the first measurement, we use the BaF detector as start with a CFD threshold of 30 mV and the mPMT as stop with a threshold of 7 mV. This leads to a standard deviation of 608 ps as can be seen in figure 3.13, which is less than desirable. Since we use a naked mPMT, the signals may be too fast for the CFD to properly process.

The time constant of the CFD was set to 2 ns in all previous setups and for all CFD channels. For the next measurement, it is changed to 1 ns for the mPMT, to see if it affects the time resolution. With the same thresholds as before and the adjusted CFD time constant we obtain a time resolution of 579 ps (see figure 3.14), which is a slight improvement but still not ideal. Changing the CFD delay time for the BaF detector signal to 1 ns as well leads to a time resolution of 660 ps and shows that the previously used 2 ns are more suitable for the BaF signal (see figure 3.15).

Another reason for the low resolution could be that the BaF light yield is too low and, similarly to the plastic scintillators used before, the 511 keV might not be enough to cause a significant number of prompt photons. To confirm this, we investigate the energy dependence of the time resolution for BaF in the next step.

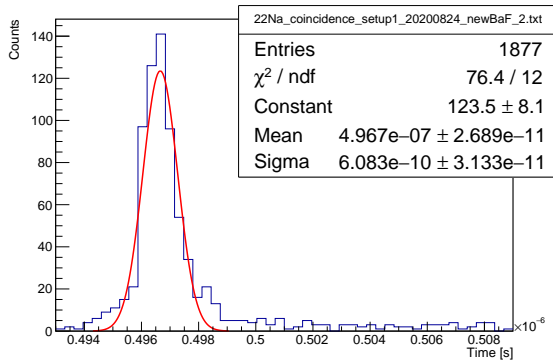


Figure 3.13.: The start signal is given by the BaF detector with a CFD threshold of 30 mV. The stop signal is given by the naked mPMT with a CFD threshold of 7 mV. The measurement is performed with a ^{22}Na source. The time resolution is 608 ps.

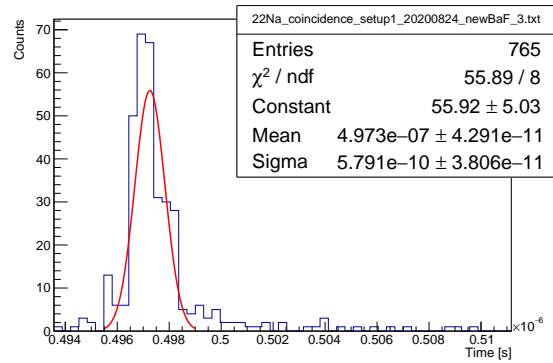


Figure 3.14.: The start signal is given by the BaF detector with a CFD threshold of 30 mV and a CFD delay time of 2 ns. The stop signal is given by the naked mPMT with a CFD threshold of 7 mV and a 1 ns delay. The measurement is performed with a ^{22}Na source. The time resolution is 579 ps.

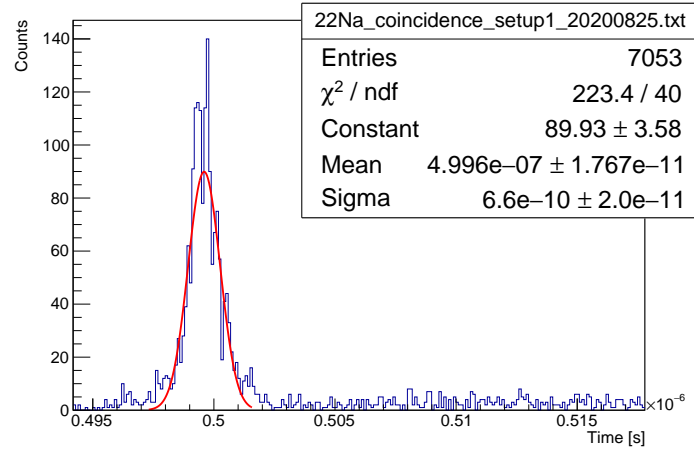


Figure 3.15.: The start signal is given by the BaF detector with a CFD threshold of 30 mV and a CFD delay time of 1 ns. The stop signal is given by the naked mPMT with a CFD threshold of 7 mV and a 1 ns delay. The measurement is performed with a ^{22}Na source. The time resolution is 660 ps.

Energy dependence of the scintillation time

To check the energy dependence of the time resolution, we measure two BaF detectors against each other using different sources. Both scintillators are of equal sizes and coupled to PMTs with similar properties. The only significant difference between both detectors is that the previously used BaF material includes filtering properties to cancel out the slow scintillation components. The newly added BaF detector does not have those properties. The results shown in figure 3.16 to 3.18 confirm the energy dependence of the resolution for the BaF scintillators as well, with a resolution of 526 ps for the ^{22}Na source and a resolution of 326 ps when measuring cosmic radiation. What we can also see, especially in figure 3.18 is a long tail in the distribution which is likely caused by the slow decay components in the BaF detector without additional filtering. Since the resolution of the ^{60}Co measurement with 347 ps (see fig. 3.17) is similar to the resolution achieved with cosmic radiation, we use the ^{60}Co source for another measurement of the BaF detector against the naked mPMT to investigate the influence of the higher energy on the whole setup. With a CFD threshold of 23 mV and a time constant of 2 ns for the BaF signal and a threshold of 7 mV and a time constant of 1 ns for the naked mPMT signal, we obtain a time resolution of 300 ps employing the ^{60}Co source (see fig. 3.19). This confirms the energy dependence of the scintillation material influences the time resolution of the entire setup.

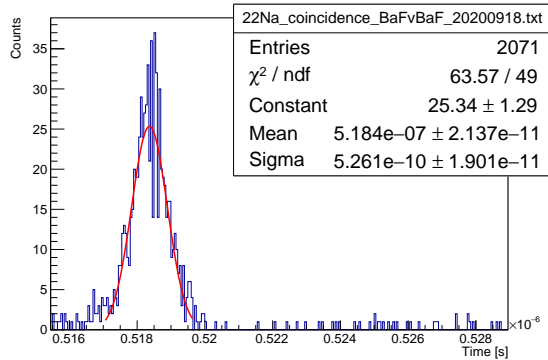


Figure 3.16.: Measuring the two BaF detectors against each other with a ^{22}Na source results in a standard deviation of 526 ps. The BaF with slow component filtering is set as the start detector with a CFD threshold of 7 mV. The BaF without filter is set as the stop detector at a CFD threshold of 8 mV. The CFD delay times are set to 2 ns for both.

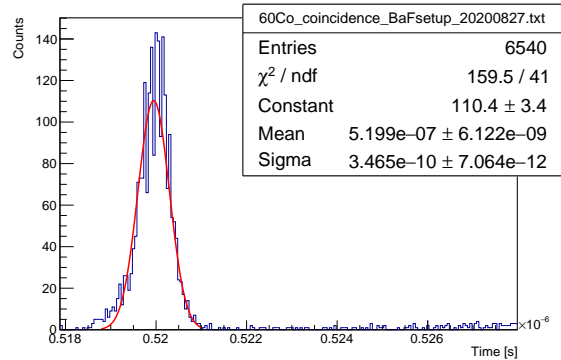


Figure 3.17.: Measuring the two BaF detectors against each other with a ^{60}Co source results in a standard deviation of 347 ps. The BaF without the slow component filter is set as the start detector with a CFD threshold of 23 mV. The BaF with filter is set as the stop detector at a CFD threshold of 22 mV. The CFD delay times are set to 2 ns for both.

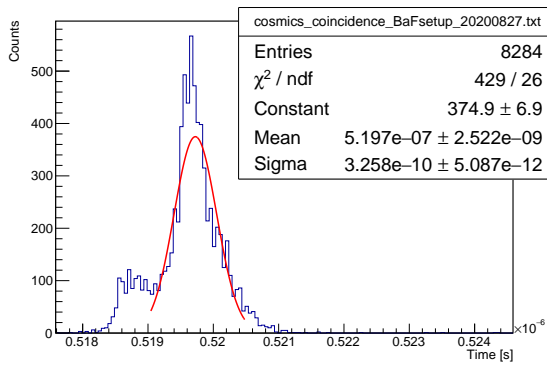


Figure 3.18.: Measuring the two BaF detectors against each other with cosmic rays results in a standard deviation of 326 ps. The BaF without the slow component filter is set as the start detector with a CFD threshold of 23 mV. The BaF with filter is set as the stop detector at a CFD threshold of 22 mV. The CFD delay times are set to 2 ns for both.

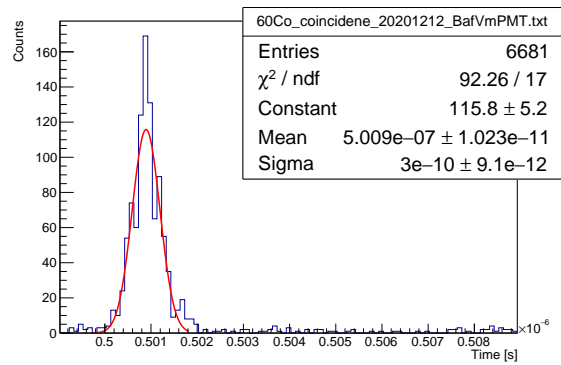


Figure 3.19.: The start signal is given by the BaF detector with a CFD threshold of 23 mV and a CFD delay time of 2 ns. The stop signal is given by the naked mPMT with a CFD threshold of 7 mV and a 1 ns delay. The measurement is performed with a ^{60}Co source. The time resolution is 300 ps.

Testing LYSO on mPMT against BaF

As a next step, we will investigate how the time distribution changes when we couple an LYSO crystal to the previously used mPMT. Since the ^{60}Co source yielded the best results so far, we use those for the upcoming measurements as well. The BaF detector with filter serves as the start detector, whereas the LYSO crystal stops the measurement. The CFD delay time is set to 2 ns for BaF and 1 ns for LYSO. The CFD thresholds are varied over several measurements, with the results shown in table 3.4.

measurement	BaF threshold	LYSO threshold	time resolution [ps]
A.11	23 mV	26 mV	458
A.12	8 mV	26 mV	563
A.13	57 mV	26 mV	625
A.14	23 mV	7 mV	852
A.15	23 mV	57 mV	413

Table 3.4.: Time resolutions yielded from measuring the LYSO and mPMT detector configuration against the BaF detector with slow component filter. The thresholds are varied over the different measurements, while the CFD delay times are set to 2 ns for BaF and 1 ns for LYSO. All measurements in this series employ a ^{60}Co source. The histograms can be found in the appendix (fig. A.11 - A.15)

The best time resolution of 413 ps is achieved with a BaF threshold of 23 mV and an LYSO threshold of 57 mV. Considering that we are already using a higher energy source, the results are unsatisfying. Another cause for the low resolution could be that we are using a multi-channel PMT with a total of 16 readout channels of which we are only using one. Therefore, we are only measuring 1/16 of the photons emitted in the scintillator, ultimately lowering the probability of detecting a lot of prompt photons. To see if this influences the resolution, we use a single-pixel PMT and LYSO crystal for the next measurements.

Measuring BaF against a single-pixel PMT coupled to LYSO

Using the same setup as before with a single-pixel PMT and equally small LYSO crystal as the stop detector yields the results shown in table 3.5. We use the BaF threshold of 23 mV which previously lead to the best results with a CFD delay time of 2 ns. The delay time for the LYSO signal is set to 1 ns while the thresholds are changed for each measurement. We can see that the time resolution with this single-pixel PMT is better for every set threshold. The best results are achieved with a 112 mV threshold on the LYSO and lead to a resolution of 338 ps. This confirms that only reading out one of

the 16 mPMT channels causes a loss in resolution. Since we do not have the option to combine all mPMT readout channels in our current setup, we should refrain from using the mPMT for a kinetics measurement.

measurement	BaF threshold	LYSO threshold	time resolution [ps]
A.16	23 mV	90 mV	346
A.17	23 mV	112 mV	338
A.18	23 mV	60 mV	358

Table 3.5.: Time resolutions yielded from measuring the LYSO and single pixel PMT detector configuration against the BaF detector with slow component filter. The thresholds are varied over the different measurements, while the CFD delay times are set to 2 ns for BaF and 1 ns for LYSO. All measurements in this series employ a ^{60}Co source. The histograms can be found in the appendix (fig. A.16 - A.18)

3.3.3. Influence of an amplitude window

Using a ^{22}Na source is generally very attractive for this setup since it is a common lab source and the detectors can easily be set up to measure the 511 keV annihilation photons with high certainty. Even though the CFD already functions in a way that the influence of an amplitude walk is minimized, a better resolution could be achieved if we only allow signals of certain pulse heights to trigger the measurement. For that reason, we implement an amplitude filter in our setup. The new setup is sketched in figure 3.20. Again, we only use NIM and CAMAC modules tested out in the previous measurements. Each detector signal now gets processed by two CAMAC CFD thresholds. The lower one is labelled as *TH1*, the higher one is *TH2*. The measurement start remains unchanged to the previous setup and is triggered by the processed *TH1* signal of the start detector. The amplitude window is implemented the same way for both detectors. *TH1* and the negated *TH2* signal are *AND*-connected, so the output of the logic modules is true only when the detector signal has an amplitude greater than *TH1* and smaller than *TH2*. If this is true for both detectors, a gate is opened by the NIM gate generator. Similarly to the previous configuration in figure 3.9, the measurement is stopped by the 1000 ns delayed *Detector 2* signal if it occurs within the open gate.

While we are still employing CAMAC and NIM modules for the CFDs which previously resulted in the best time resolutions, their configuration has changed quite significantly, which is why we first proceed with another measurement to evaluate the time resolution of the electronic components. Like in previous measurements with that purpose, we use the same detector signal as the input for all CFD channels. Using a ^{22}Na source and the LYSO pixel detector, we adjust the thresholds in such a way that they only allow the

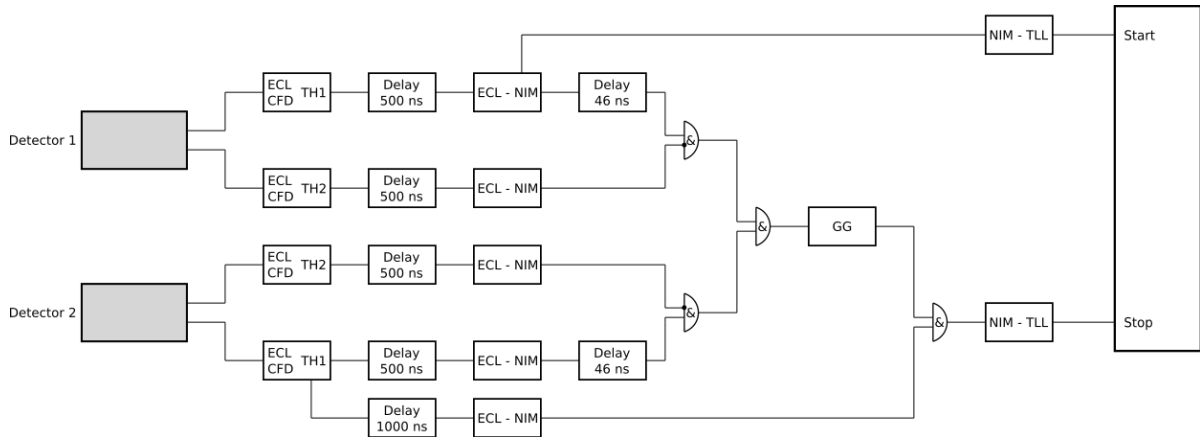


Figure 3.20.: Schematic setup of the electronic components used for the coincidence timing measurements with an amplitude window. For the amplitude window both detector signals are split and processed by a lower ($TH1$) and higher ($TH2$) CAMAC CFD threshold. Additionally, the $TH1$ signal is delayed by a NIM module to compensate any time delays caused by the negation of the $TH2$ signal. If both detector signal amplitudes are within the window set by $TH1$ and $TH2$, respectively, a gate is opened. If the 1000 ns delayed $TH1$ signal of *Detector 2* occurs within the open gate, then the measurement is stopped.

511 keV peak to trigger the measurement, which results in a lower threshold of 27 mV and a higher threshold of 33 mV for the start and stop signal. This results in a time resolution of the electronic components of 81 ps.

With this knowledge, we can proceed to measure the two BaF detectors against each other using a ^{22}Na source with an amplitude window around the 511 keV photon signals to see if it improves the resolution. This is done for the measurement results shown in 3.22. With the BaF without slow component filtering and threshold of 8 mV and 22 mV as the start detector and the BaF with filter and thresholds of 30 mV and 48 mV, we obtain a time resolution of 501 ps. We can compare this result to a previous measurement of the same two detectors with a sodium source without the amplitude window, which lead to a time resolution of 526 ps. Even though we can see a slight improvement, the amplitude window does not enable the BaF detectors to function as a start detector in a high-resolution measurement with a low energy source.

As a possible alternative for a start detector, we proceed with a measurement series using the LYSO pixel. However, the results in table 3.6 show no improvement in the resolution when we employ the LYSO pixel detector in a measurement against the mPMT, regardless of the amplitude window. This leads to the temporary conclusion that even though the light yield is relatively low and we have an evident loss in resolution when measuring with a sodium source, the BaF detector as the measurement start seems to lead to the best results.

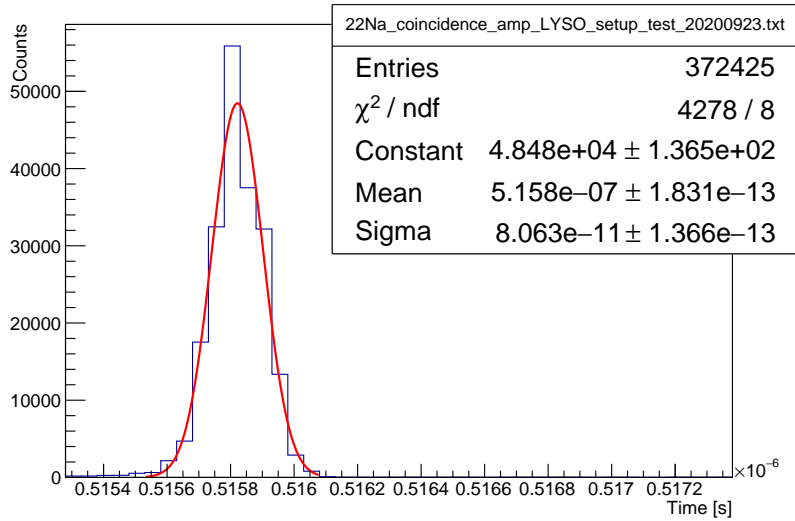


Figure 3.21.: Using a ^{22}Na source and the pixel LYSO detector with an amplitude window around the 511 keV peak ($TH1=27$ mV, $TH2=23$ mV) for the start and stop signal yields a time resolution of 81 ps for the electronic components of the amplitude window configuration sketched in figure 3.20.

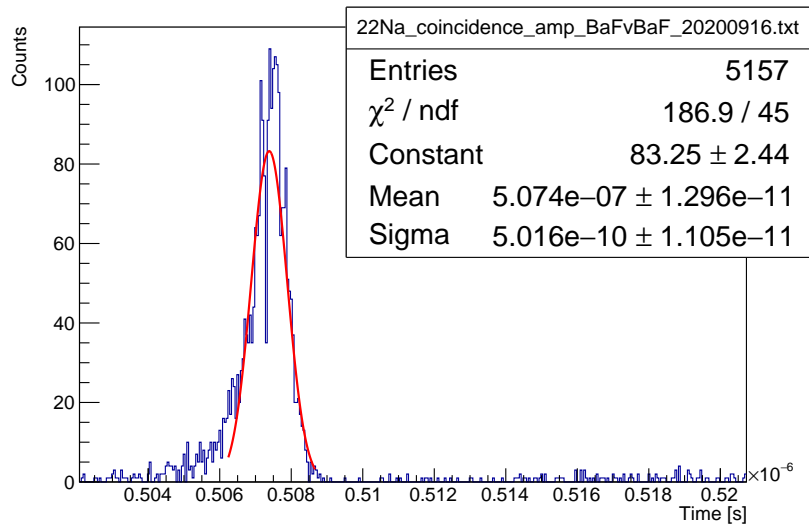


Figure 3.22.: Measuring the two BaF detectors against each other with a ^{22}Na source. The BaF detector without filter gives the start signal with $TH1=8$ mV and $TH2=22$ mV. The BaF with slow component filtering serves as the stop detector with $TH1=30$ mV and $TH2=48$ mV. The time resolution is 501 ps.

	LYSO TH1	LYSO TH2	Dec2	Det2 TH1	Det2 TH2	time resolution
A.19	27 mV	33 mV	BaF	30 mV	41 mV	497 ps
A.20	27 mV	955 mV	BaF	30 mV	955 mV	481 ps
A.21	26 mV	33 mV	mPMT	8 mV	955 mV	558 ps
A.20	7 mV	955 mV	mPMT	8 mV	955 mV	641 ps

Table 3.6.: Time resolutions yielded from the measurement series with the LYSO pixel detector. It is measured against the BaF with slow component filtering and the mPMT, both known from previous measurements. Each measurement is performed with and without the amplitude window. The corresponding histograms can be found in the appendix section A.4 (fig. A.19 - A.22)

New PMT measurements

At this point in the project, a new PMT has become available, which is optimized for high-resolution timing measurements. Performing a measurement with the previously used BaF as the start detector and the new, naked PMT as the stop detector leads to the results shown in table 3.7. Immediately, we can see a great improvement in the time resolution. However, we can also notice another influencing factor. As we have seen in the previous section, the small amplitude window around the 511 keV photon peak has not lead to significant improvement of the resolution. However, we still employ the amplitude window setup from figure 3.20. In the first measurement presented in table 3.7 we set the BaF thresholds in a way that we do not measure any signal lower than the 511 keV signals. As the higher threshold, we use the maximum value that can be set with the used CFD. While this leads to a bigger amplitude window, we still cut off any signals with pulse heights higher than the maximum 955 mV, which leads to a significantly better time resolution of 178 ps than the one yielded from measurements without an amplitude window altogether. The resolution of 235 ps is received in a measurement using the setup from figure 3.9 with no amplitude window.

With the new PMT and knowing that the amplitude window used in such a way leads to better results, we can now use the BaF detector in first kinetics measurements.

	BaF TH1	BaF TH2	PMT TH1	PMT TH2	time resolution
A.23	26 mV	966 mV	8 mV	954 mV	178 ps
A.24	30 mV	–	8 mV	–	235 ps

Table 3.7.: Time resolutions yielded from the measurements with the new PMT against the BaF detector with slow component filtering. (fig. A.19 - A.22)

3.4. Final Setup

The final setup of this project differs slightly from the previously used amplitude setup in figure 3.20. As can be seen in the schematic 3.23, the signal processing for the start detector still features the amplitude window that leads to the best results so far, set by $TH1$ and $TH2$. Using BaF as a start detector, $TH1$ is set slightly lower than the pulse height resulting from 511 keV photons, while $TH2$ is set to the maximum value given by the CFD. For *Detector 2* we couple the scintillation material we want to characterize to the fast PMT. Since we want to measure the full kinetic spectrum, we do not include any amplitude filters here, and the CFD threshold is at the lowest possible setting. This reduces the signal processing components for the stop signal to a single CFD channel, the CAMAC delay module and the signal conversion. The time response of the electronic components is characterized according to previous methods and results in a resolution of 84 ps.

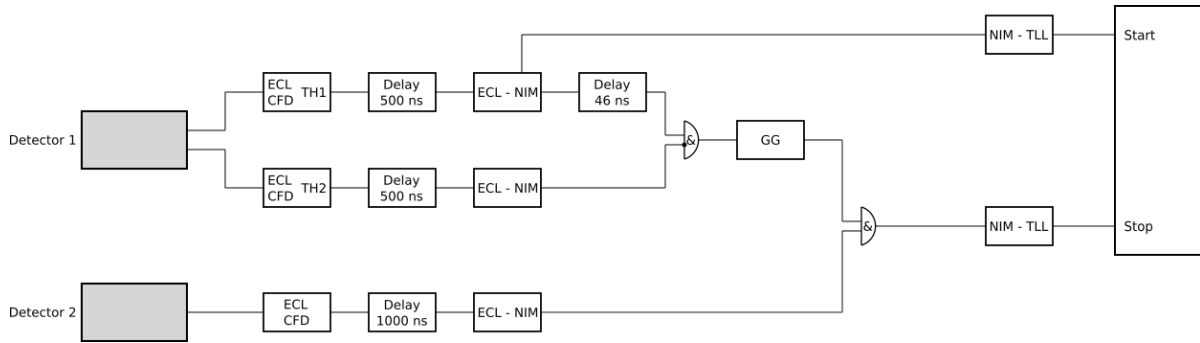


Figure 3.23.: Schematic of the final measurement setup used. *Detector 1* is the set start detector with the known time response. *Detector 2* is the PMT coupled to the scintillation material of which we want to measure the kinetics. For *Detector 1* the amplitude window can be adjusted by the CFD thresholds $TH1$ (low) and $TH2$ (high). A signal within that window will open the coincidence gate. The start signal is given by the $TH1$ *Detector 1* signal. The measurement stop is triggered when the *Detector 2* signal occurs within the coincidence gate.

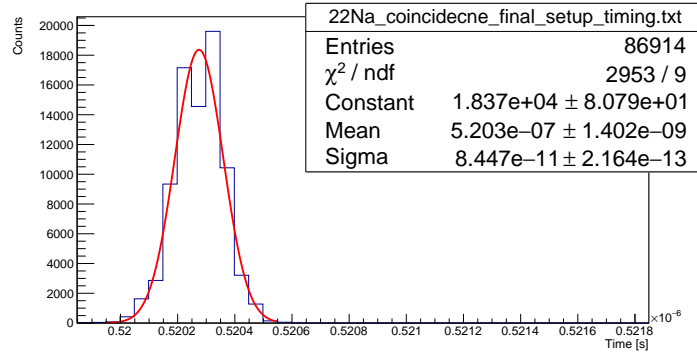


Figure 3.24.: Measurement to characterize the jitter caused by the electronic components used in the configuration shown in figure 3.23. The time resolution is 84 ps.

3.4.1. Measuring LYSO against BaF

For the first scintillation kinetics measurement, we measure an LYSO crystal coupled to the fast PMT against the BaF detector. The CFD amplitude window for the BaF signal is set to $TH1=30$ mV and $TH2=966$ mV. The LYSO threshold is set to 8 mV which is the lowest setting on the CFD. The results shown in figure 3.25 are obtained by measuring with a sodium source. Since we are now no longer primarily interested in the time resolution but rather the scintillation decay time of the LYSO crystal, we fit the resulting LYSO slope with an exponential function. The fit gives a slope of -1.87×10^9 1/s. We know from the theoretical prerequisites in chapter 2 that the scintillation kinetics can be described by an exponential function, where the exponent is given by $1/\tau$, with τ being the decay time. Therefore, the inverted slope obtained by the exponential fit gives information about the materials decay time. For the measured LYSO slope in 3.25, we obtain a decay time of about 535 ps.

Due to a lack of information about the crystal used in these measurements, it is difficult to judge the credibility of the result. As has been discussed in section 2.2.2, the decay time of a scintillator is heavily dependent on its material components. The detailed material composition of the used crystal is unknown; therefore, we cannot predict a decay time independent of the measurement.

3.4.2. Measuring PWO against BaF

The same measurement is performed with a PWO crystal attached to the PMT. The CFD thresholds remain unchanged to the previous measurement with $TH1=30$ mV and $TH2=966$ mV for the BaF and 8 mV for the PWO signal. The results are displayed in figure 3.26. The exponential fit to the PWO slope results in -2.18×10^9 1/s, which leads to a decay time of 459 ps. If we plot the obtained data with a logarithmic scale for the y-axis, we can see that the overall decay time of the crystal probably contains

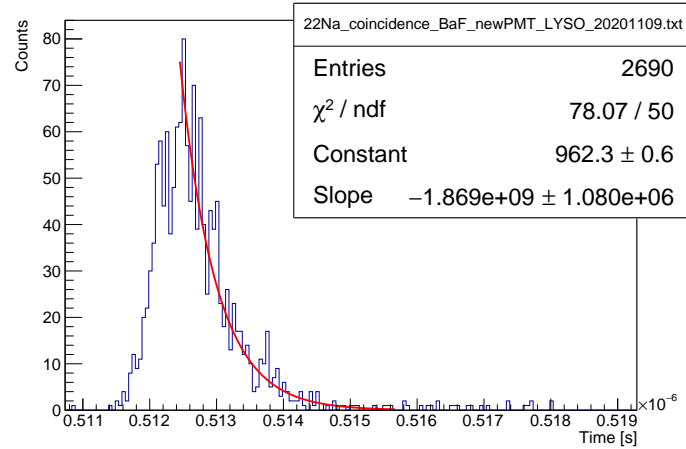


Figure 3.25.: Measurement with a ^{22}Na source of an LYSO crystal coupled to a PMT against the BaF detector with the setup shown in 3.23. The thresholds for the BaF signal are $TH1=30$ mV and $TH2=966$ mV. The threshold for the LYSO signal is 8 mV. An exponential fit to the LYSO slope results in a slope of -1.87×10^9 1/s.

two time components. Fitting those two separately, which is done in figure 3.27 and 3.28, we obtain the two different decay times. The first slope of -2.16×10^9 1/s yields a time constant of 463 ps, similar to the overall time constant obtained from the fit in figure 3.26. The second fit results in a slope of -7.5×10^8 1/s yielding a time constant of 1.3 ns. Similarly to the LYSO crystal, the complete material composition of the PWO crystal is unknown, which is why it is difficult to compare the results to the decay times of other PWO scintillators.

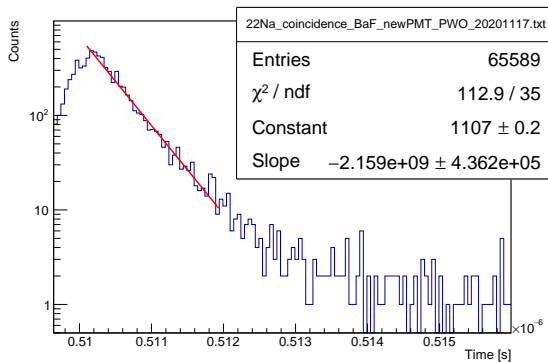


Figure 3.27.: An exponential fit to the first possible PWO decay components yields a slope of -2.16×10^9 1/s, or a decay constant of 463 ps.

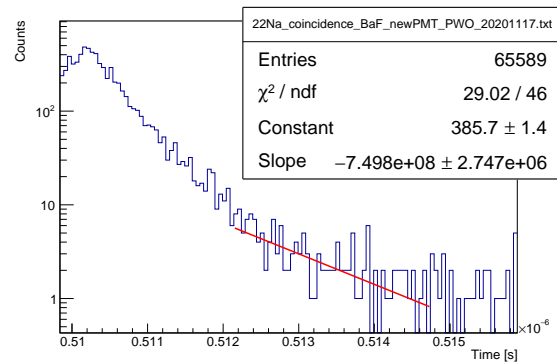


Figure 3.28.: An exponential fit to the first possible PWO decay components yields a slope of -7.5×10^8 1/s, or a decay constant of 1.3 ns.

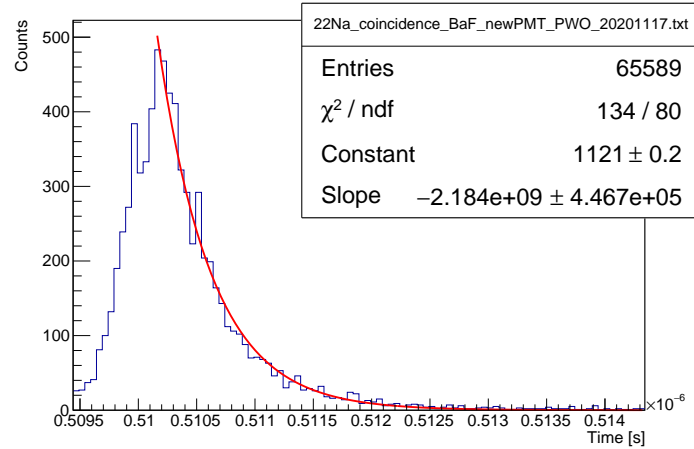


Figure 3.26.: Measurement with a ^{22}Na source of a PWO crystal coupled to a PMT against the BaF detector with the setup shown in 3.23. The thresholds for the BaF signal are $TH1=30$ mV and $TH2=966$ mV. The threshold for the PWO signal is 8 mV. An exponential fit to the PWO slope results in a slope of -2.18×10^9 1/s.

Another observation resulting from the LYSO and PWO results is that we only seem to be able to measure the fast decay components. While this generally speaks in favor of the resolution we have been able to achieve with this setup, it also suggests that we are not able to measure the full scintillation time spectra of our materials. Considering this is what we want to measure, further adjustments to the setup are needed to achieve that goal. A possible reason we only measure the fast decay times could be that the dead time of the PMT cuts off all slower photons. Lowering the overall photon statistic through geometric changes to the setup could potentially allow us to measure the full spectrum. Perhaps the previously used mPMT could be a solution as well since we can only read out one of 16 channels, which automatically results in a lower photon statistic. However, further experiments are needed to confirm this and develop a final setup.

4. Conclusion and outlook

Throughout this thesis, we were able to develop and characterize a coincidence measurement system with the highest possible time resolution achievable with our lab resources. The optimization process was split into two parts: the electronic and the detector components. Testing various NIM and CAMAC CFD modules and their configurations in a coincidence measurement setup, we were able to reach a resolution of 57 ps. Here, the CAMAC CFD and Delay modules proved to be the most precise.

The central part of this thesis was spent on finding the ideal start detector and its configuration in the setup. A barium-fluoride scintillator with additional material components to filter out the scintillation photons resulting from slower decay times coupled to a PMT yielded the best results. However, an apparent energy dependence of the time response was observed with the highest resolution of 180 ps resulting from measuring cosmic radiation with two BaF detectors. Even though the BaF light yield is low for low energy photons like 511 keV annihilation photons emitted from a ^{22}Na source, we still prefer the sodium source over cosmic radiation for among others, fast attainment of sufficient statistics.

Furthermore, we implemented an amplitude window to filter out detector signals which do not correspond to the particle energies which should trigger the measurements. This led to small improvements to the resolution, especially when the window was set in such a way that we cut off all noise but also cut all signals with pulse amplitudes larger than the highest CFD threshold.

Testing different photodetectors against the BaF detector, we concluded that using a multichannel PMT is not ideal in the developed setup since we can only read out one of the multiple channels, causing a loss in prompt photon statistics and thus, a worse time resolution. The best results were obtained with a single channel PMT optimized for fast timing measurements and led to a resolution of 180 ps, including the BaF, electronics and PMT influences.

Testing the system by measuring the scintillation kinetics of an LYSO and PWO crystal showed that we seem to cut off the slower scintillation decay time components of the materials. This is likely caused by the PMT dead time because we predominantly measure prompt photons. To avoid this, we might be able to use the lowered photon statistics of the mPMT to our advantage, even though the overall resolution might decrease. Another option would be to develop a new geometric configuration which would lower the detection rate of prompt photons but still employ the PMT with the best timing response.

While further research and measurements are needed to develop a high-resolution setup

capable of characterizing a full scintillation time spectrum, we were nevertheless able to develop a high-resolution measurement setup successfully.

Further experiments using this setup and the knowledge we obtained over the course of this thesis could also be directed towards the 10 ps challenge which is about high-resolution time-of-flight measurements, possibly benefitting current research in *positron emission tomography*. For this purpose, we would perform different measurements with the two BaF detectors, unequally changing the distance of each detector to the sodium source to investigate changes in the produced time distribution.

A. Appendix

A.1. Additional measurement results for section 3.1

Setup 1

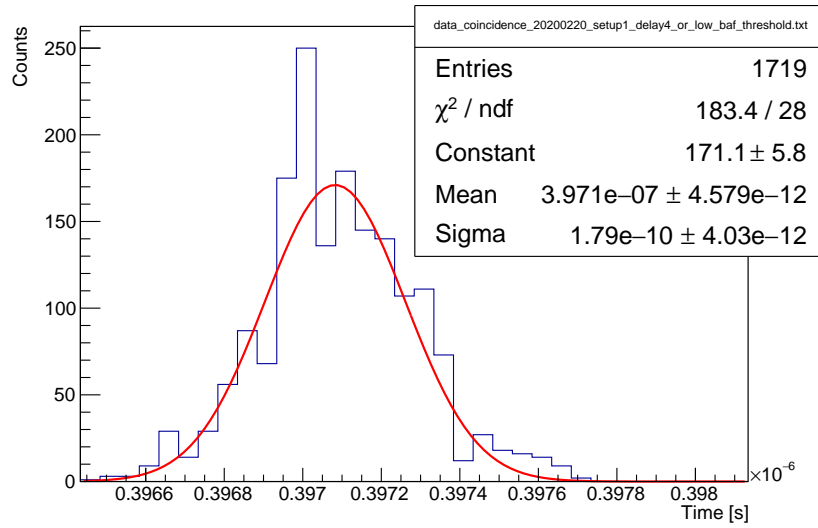


Figure A.1.: Setup 1 with delay module 4 and OR connected plastic detectors yields a time resolution of about 179 ps.

Setup 2

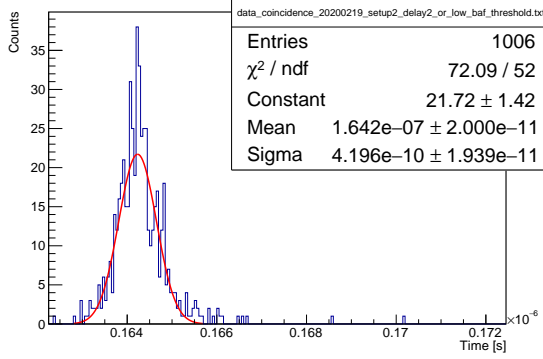


Figure A.2.: Setup 2 with delay module 2 and OR connected plastic detectors yields a time resolution of about 420 ps.

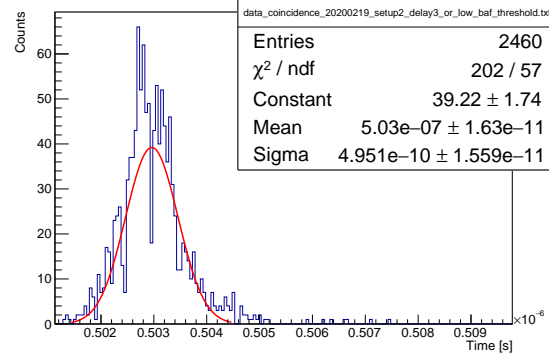


Figure A.3.: Setup 2 with delay module 3 and OR connected plastic detectors yields a time resolution of about 495 ps.

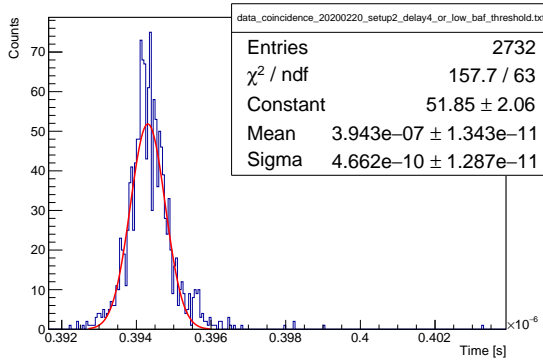


Figure A.4.: Setup 2 with delay module 4 and OR connected plastic detectors yields a time resolution of about 466 ps.

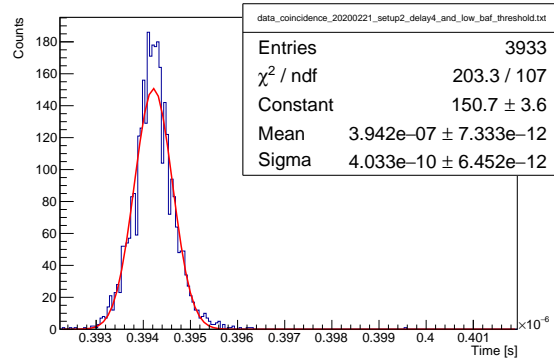


Figure A.5.: Setup 2 with delay module 4 and AND connected plastic detectors yields a time resolution of about 403 ps.

Setup 3

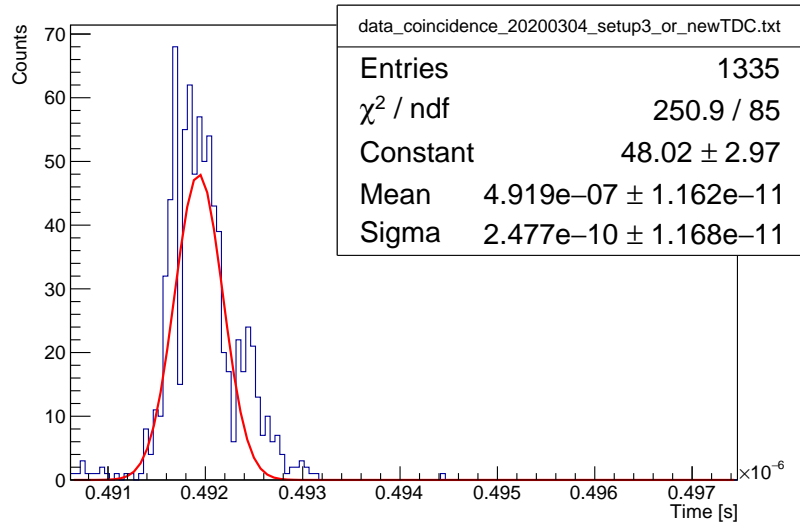


Figure A.6.: Setup 3 with OR connected plastic detectors yields a time resolution of about 248 ps.

A.2. Additional measurement results for section 3.3.1

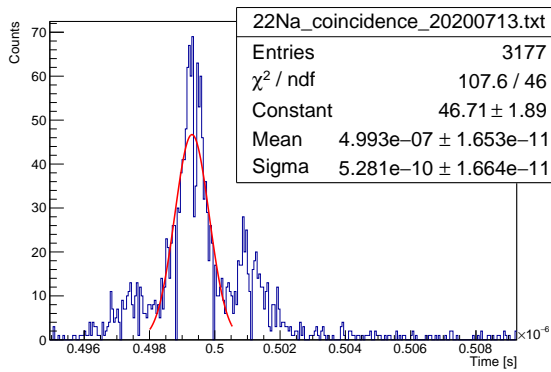


Figure A.7.: Measuring two plastic detectors against each other with a ^{22}Na source leads to a time resolution of 528 ps.

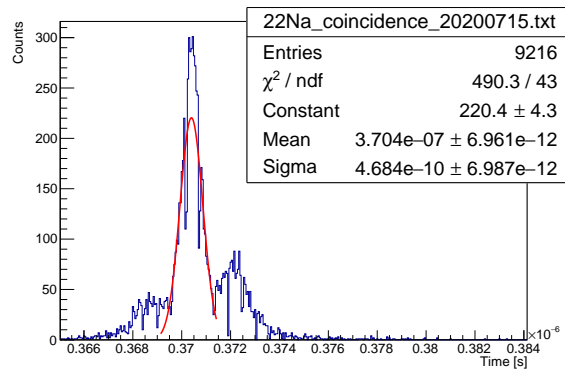


Figure A.8.: Measuring two plastic detectors against each other with a ^{22}Na source leads to a time resolution of 468 ps.

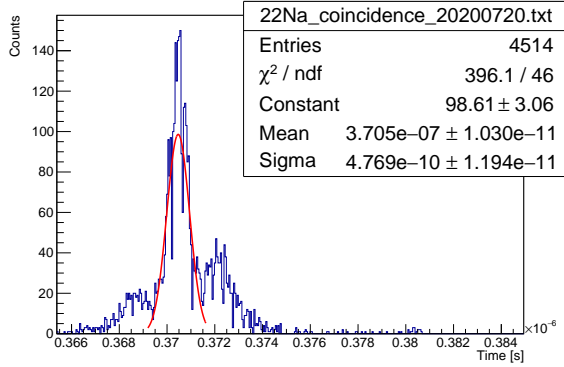


Figure A.9.: Measuring two plastic detectors against each other with a ^{22}Na source leads to a time resolution of 477 ps.

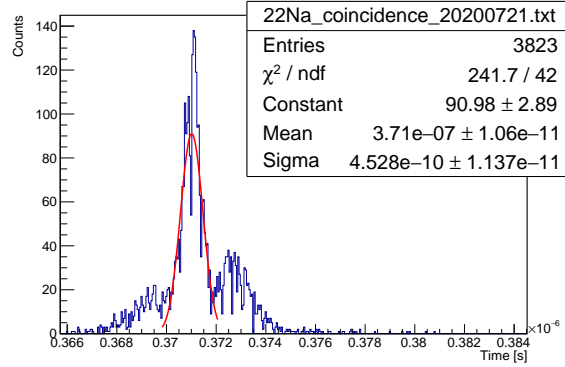


Figure A.10.: Measuring two plastic detectors against each other with a ^{22}Na source leads to a time resolution of 453 ps.

A.3. Additional measurements for section 3.3.2

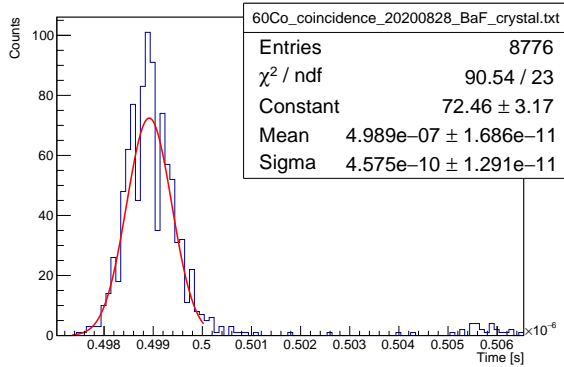


Figure A.11.: Measurement with a ^{60}Co source. BaF with slow component filter as start. LYSO coupled to mPMT as stop. The BaF CFD threshold is 23 mV with a CFD time constant of 2 ns. The LYSO CFD threshold is 26 mV with a CFD time constant of 1 ns. This yields a time resolution of 458 ps.

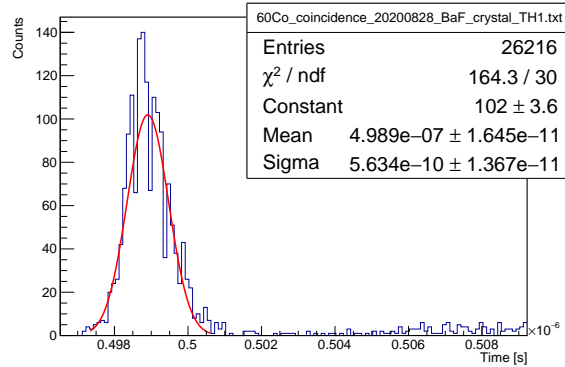


Figure A.12.: Measurement with a ^{60}Co source. BaF with slow component filter as start. LYSO coupled to mPMT as stop. The BaF CFD threshold is 8 mV with a CFD time constant of 2 ns. The LYSO CFD threshold is 26 mV with a CFD time constant of 1 ns. This yields a time resolution of 563 ps.

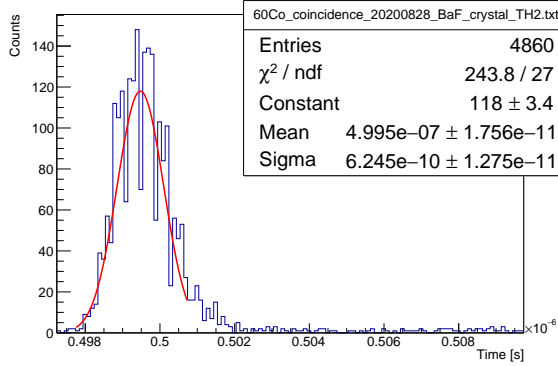


Figure A.13.: Measurement with a ^{60}Co source. BaF with slow component filter as start. LYSO coupled to mPMT as stop. The BaF CFD threshold is 57 mV with a CFD time constant of 2 ns. The LYSO CFD threshold is 26 mV with a CFD time constant of 1 ns. This yields a time resolution of 625 ps.

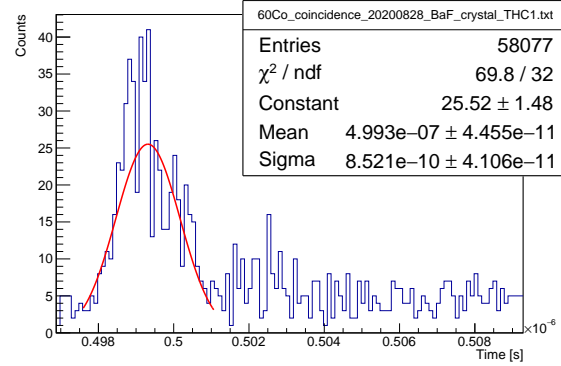


Figure A.14.: Measurement with a ^{60}Co source. BaF with slow component filter as start. LYSO coupled to mPMT as stop. The BaF CFD threshold is 23 mV with a CFD time constant of 2 ns. The LYSO CFD threshold is 7 mV with a CFD time constant of 1 ns. This yields a time resolution of 852 ps.

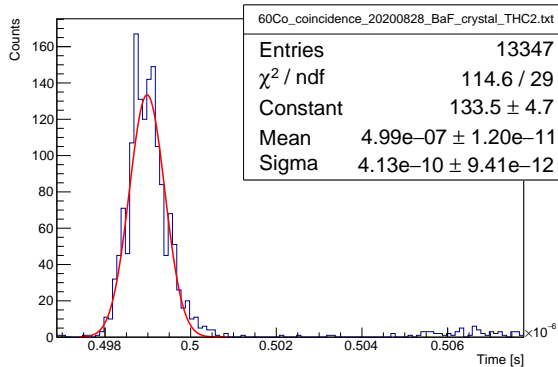


Figure A.15.: Measurement with a ^{60}Co source. BaF with slow component filter as start. LYSO coupled to mPMT as stop. The BaF CFD threshold is 23 mV with a CFD time constant of 2 ns. The LYSO CFD threshold is 57 mV with a CFD time constant of 1 ns. This yields a time resolution of 413 ps.

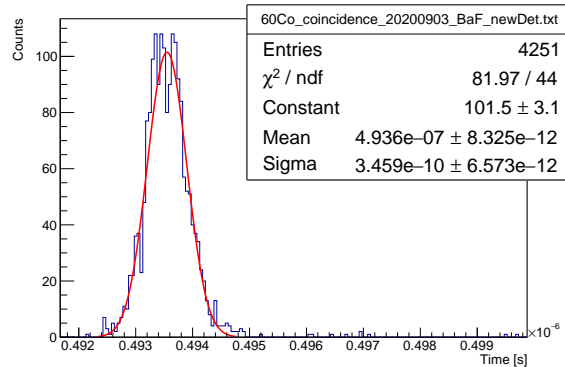


Figure A.16.: Measurement with a ^{60}Co source. BaF with slow component filter as start. LYSO coupled to single pixel PMT as stop. The BaF CFD threshold is 23 mV with a CFD time constant of 2 ns. The LYSO CFD threshold is 90 mV with a CFD time constant of 1 ns. This yields a time resolution of 346 ps.

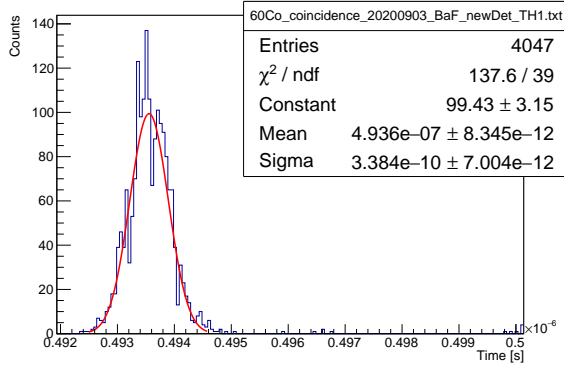


Figure A.17.: Measurement with a ^{60}Co source. BaF with slow component filter as start. LYSO coupled to single pixel PMT as stop. The BaF CFD threshold is 23 mV with a CFD time constant of 2 ns. The LYSO CFD threshold is 112 mV with a CFD time constant of 1 ns. This yields a time resolution of 338 ps.

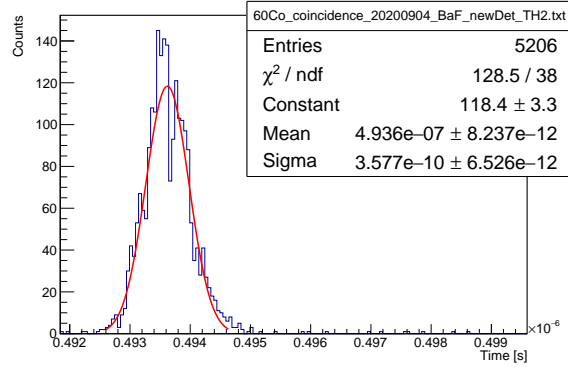


Figure A.18.: Measurement with a ^{60}Co source. BaF with slow component filter as start. LYSO coupled to single pixel PMT as stop. The BaF CFD threshold is 23 mV with a CFD time constant of 2 ns. The LYSO CFD threshold is 60 mV with a CFD time constant of 1 ns. This yields a time resolution of 358 ps.

A.4. Additional measurements for section 3.3.3

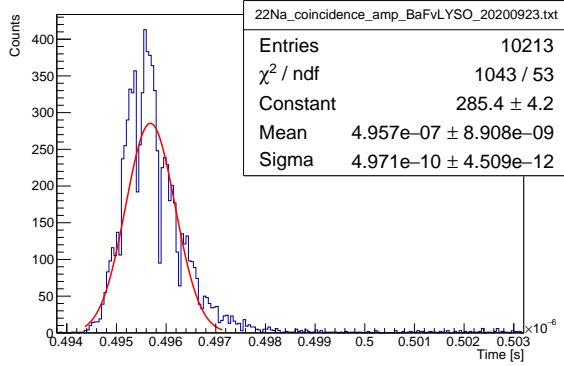


Figure A.19.: Measurement with a ^{22}Na source. BaF with slow component filter as start. LYSO coupled to single pixel PMT as stop. The amplitude window is set as follows: For BaF: $TH1=30$ mV, $TH2=41$ mV. For LYSO: $TH1=27$ mV, $TH2=33$ mV. This leads to a time resolution of 497 ps.

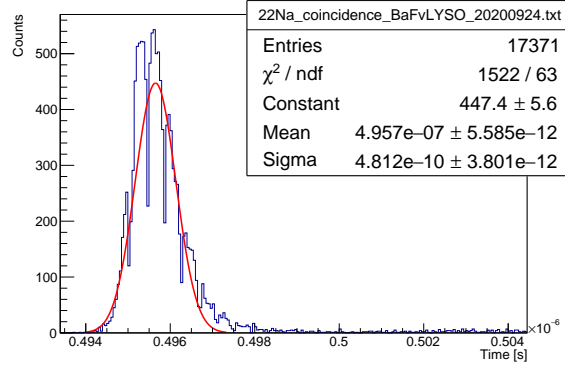


Figure A.20.: Measurement with a ^{22}Na source. BaF with slow component filter as start. LYSO coupled to single pixel PMT as stop. The amplitude window is set as follows: For BaF: $TH1=30$ mV, $TH2=955$ mV. For LYSO: $TH1=27$ mV, $TH2=955$ mV. This leads to a time resolution of 481 ps.

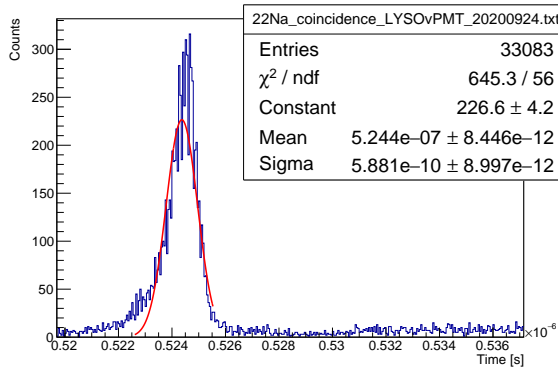


Figure A.21.: Measurement with a ^{22}Na source. LYSO coupled to single pixel PMT as start. Naked mPMT as stop. The amplitude window is set as follows: For LYSO: $TH1=26$ mV, $TH2=33$ mV. For mPMT: $TH1=8$ mV, $TH2=955$ mV. This leads to a time resolution of 588 ps.

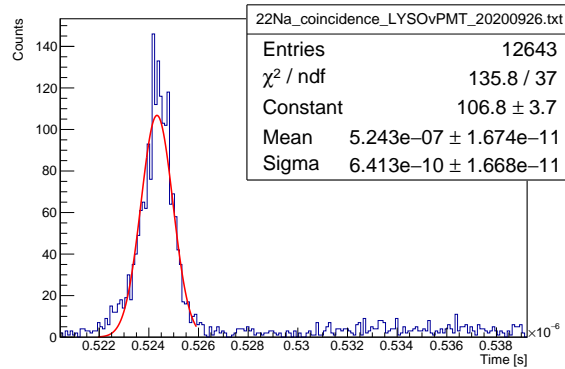


Figure A.22.: Measurement with a ^{22}Na source. LYSO coupled to single pixel PMT as start. Naked mPMT as stop. The amplitude window is set as follows: For LYSO: $TH1=7$ mV, $TH2=955$ mV. For mPMT: $TH1=8$ mV, $TH2=955$ mV. This leads to a time resolution of 641 ps.

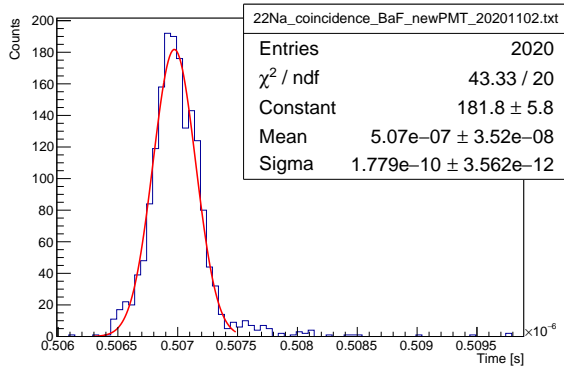


Figure A.23.: Measurement with a ^{22}Na source. BaF with slow component filter as start. Naked, new PMT as stop. The amplitude window is set as follows: For BaF: $TH1=26$ mV, $TH2=966$ mV. For PMT: $TH1=8$ mV, $TH2=954$ mV. This leads to a time resolution of 178 ps.

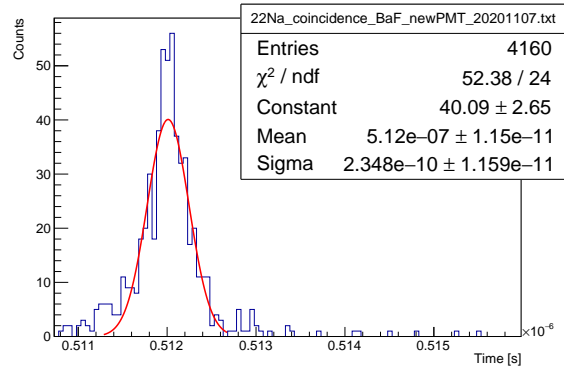


Figure A.24.: Measurement with a ^{22}Na source. BaF with slow component filter as start. Naked, new PMT as stop. The configuration in 3.9 is used with a BaF threshold of 30 mV and a PMT threshold of 7 mV. This leads to a time resolution of 235 ps.

Bibliography

- [1] T. Hebbeker and K. Hoepfner. „Muon Spectrometers“. In: *Handbook of Particle Detection and Imaging*. Ed. by C. Grupen and I. Buvat. Berlin, Heidelberg: Springer Berlin Heidelberg, 2012, pp. 473–496. DOI: 10.1007/978-3-642-13271-1_19.
- [2] P. Zyla et al. „Review of Particle Physics“. In: *PTEP* 2020.8 (2020), p. 083C01. DOI: 10.1093/ptep/ptaa104.
- [3] G. F. Knoll. *Radiation detection and measurement*. New York [u.a.], 1989.
- [4] H. Kolanoski and N. Wermes. *Teilchendetektoren*. Springer Berlin Heidelberg, 2016. DOI: 10.1007/978-3-662-45350-6.
- [5] H. U. Schmidt. *Meßelektronik in der Kernphysik*. Stuttgart, 1986.
- [6] *TDC7200 Time-to-Digital Converter for Time-of-Flight Applications in LIDAR, Magnetostrictive and Flow Meters*. SNAS647D. revised 03/2016. Mar. 2015.
- [7] S. Landsberger. *Measurement and Detection of Radiation, Third Edition*. 3rd ed. Baton Rouge, 2013.
- [8] *Multianode Photomultiplier Tube Assembly*. H6568, H6568-10. July 2001.

Selbstständigkeitserklärung

Hiermit versichere ich, die vorgelegte Thesis selbstständig und ohne unerlaubte fremde Hilfe und nur mit den Hilfen angefertigt zu haben, die ich in der Thesis angegeben habe. Alle Textstellen, die wörtlich oder sinngemäß aus veröffentlichten Schriften entnommen sind, und alle Angaben die auf mündlichen Auskünften beruhen, sind als solche kenntlich gemacht. Bei den von mir durchgeführten und in der Thesis erwähnten Untersuchungen habe ich die Grundsätze guter wissenschaftlicher Praxis, wie sie in der ‚Satzung der Justus-Liebig-Universität zur Sicherung guter wissenschaftlicher Praxis‘ niedergelegt sind, eingehalten. Gemäß § 25 Abs. 6 der Allgemeinen Bestimmungen für modularisierte Studiengänge dulde ich eine Überprüfung der Thesis mittels Anti-Plagiatssoftware.

Datum

Unterschrift